Supplementary Information for:

Efficient mechanochemistry of beta blockers: Neutralization, salification, and effect of liquid additives

Delbert S. Botes,[ab] Jesus Daniel Loya,[b] Mahboubeh Ghahremani,[b] Bailee B. Newham,[b] Mikaela I. Aleman,[b] Gary C. George III,[ab] Daniel K. Unruh[b] and Kristin M. Hutchins*[abc]

[a]Department of Chemistry, University of Missouri, 601 S College Avenue, Columbia, Missouri, 65211, United States.

[b]Department of Chemistry & Biochemistry, Texas Tech University, 1204 Boston Avenue, Lubbock, Texas 79409, United States.

[c]MU Materials Science & Engineering Institute, University of Missouri, Columbia, Missouri, 65211, United States.

*Email: kristin.hutchins@missouri.edu

Table of Contents:

1. Supplementary tables

Table S1: CSD search results*

Beta blocker	Coformer	CSD refcode	Space group	Beta blocker form/ type of crystals
Propranolol	N/A, Free base	IMITON[1]	$P2_1$	*S*-propranolol
		PROPRA10[2]	$P2_1/c$	Racemate
	Capric Acid	YAYNAR[3]	*P*-1	Racemate
	Fumaric Acid	HUZPOJ[4]	*P*-1	Racemate
		HUZPUP[4]	*P*-1	Racemate
	Hydrobromic Acid	FEHXIA[5]	$P2_1$	Racemate
	Hydrochloric Acid	FIDGAB[5]	$P2_1$	Racemate
		PROPDD[6]	$P2_1$	*D*-propranolol
		PROPDL01[7]	$P2_1/c$	Racemate
		PROPDL10[2]	$P2_1/n$	Racemate
	Hydrofluoric Acid	FEHXEW[5]	$P2_1$	Conglomerate
	Hydroiodic Acid	FEHXOG[5]	*P*-1	Racemate
	Maleic Acid	HUZQAW[4]	$P2_1/n$	Racemate
	Nitric Acid	ROZXAG[8]	*P*-1	Racemate
	Oxalic Acid	HUZQEA[4]	$P2_1$	Conglomerate
		HUZQIE[4]	$Pbn2_1$	Racemate
		HUZQOK[4]	$P2_1/c$	Racemate
	Sebacic Acid	EROJED[9]	*P*-1	Racemate
Metoprolol	N/A, Free base	XITNIA[10]	$P2_1/n$	Racemate
		XITNIA01[11]	$P2_1/n$	Racemate
	3,5-Dinitrobenzoic Acid	TILNUB[12]	*P*-1	Racemate
	4-Hydroxybenzoic Acid	TILPAJ[12]	$P2_1/c$	Racemate
	Chlorobenzoic Acid	TILNIP[12]	*P*-1	Racemate
	Cinnamic Acid	TILNOV[12]	$P2_1/c$	Racemate
	Dihydrocaffeic Acid	TILNAH[12]	*P*-1	Racemate
	Fumaric Acid	AGOVIE[13]	$P2_1/c$	Racemate
	Nicotinic Acid	TOPZIK[13]	*P*-1	Racemate
	Oxalic Acid	TILNEL[13]	$P2_1/n$	Racemate
	Succinic Acid	YOTXOV[14]	$P2_1/c$	Racemate
	Tartaric Acid	ZUYJOU[15]	$P2_122_1$	Racemate
Acebutolol	Hydrochloric Acid	ACBUOL[16]	$C2/c$	Racemate
	Tetraphenylborate	TANGUN[17]	$P2_1/c$	Racemate
Atenolol	N/A, Free base	CEZVIN[18]	$C2/c$	Racemate
		CIDHAZ[18]	$C2$	*S*-atenolol
	4-Aminobenzoic Acid	JIRWIR[19]	$C2/c$	Racemate
	BINOL-phosphoric Acid	QAJYIL[20]	$Pna2_1$	Racemate
	Hydrochloric Acid	WEWLOC[21]	$P2_1/c$	Racemate
	Succinic Acid	DETHIU[22]	$P2_1/c$	Racemate
Labetalol	Hydrochloric Acid	CEZJOG[23]	$P2_12_12_1$	*R,R*-labetalol

*Searches were conducted using Conquest with CSD Version 5.45 (November 2023) with 2 updates (March and June 2024).

Table S2: pK_a calculations[a]

Beta blocker		Nicotinic Acid		Isonicotinic Acid	
Name	**pK_a**	**pK_a**	**ΔpK_a[b]**	**pK_a**	**ΔpK_a[b]**
Propranolol	9.27	2.31	6.96	2.01	7.26
Metoprolol	9.27		6.96		7.26
Acebutolol	9.25		6.94		7.24
Atenolol	9.27		6.96		7.26
Labetalol	9.80		7.49		7.79

[a]pK_a values were determined using the protonation pK_a calculator in MarvinSketch 23.12[24] with the default options selected.

[b]ΔpK_a = pK_a(protonated beta blocker base) - pK_a(acid: Nicotinic Acid/Isonicotinic Acid). If the ΔpK_a value is less than -1, cocrystals are predicted to form while a difference greater than 3 or 4 predicts salt formation. Values lying between -1 and 3 or 4 lie in the salt-cocrystal continuum where either can result.[25, 26]

2. Materials and methods

2.1 Materials

Metoprolol tartrate (**Met tartrate**), atenolol (**Ate**), and nicotinic acid (**NA**) were purchased from Tokyo Chemical Industry Co., Ltd (Toshima, Kita, Tokyo, Japan). Acebutolol hydrochloride (**Ace HCl**) was purchased from Alfa Aesar (Ward Hill, MA, USA) while propranolol hydrochloride (**Pro HCl**), and isonicotinic acid (**INA**) were purchased from Oakwood Chemical (Estill, SC, USA). Additional **Ate** and **Ace HCl** were purchased from Combi-Blocks (San Diego, CA, USA). Labetalol hydrochloride (**Lab HCl**) was purchased from Sigma-Aldrich (St. Louis, MO, USA) and AA Blocks (San Diego, CA, USA). All solvents namely acetone, acetonitrile, chloroform, dichloromethane, diethyl ether, *N*,*N*-dimethylformamide, ethanol, ethyl acetate, hexanes, isopropanol, methanol, tetrahydrofuran and toluene were purchased from Fisher Scientific (Lenexa, KS, USA). Reagents and solvents were used as received without further purification.

2.2 Mechanochemistry

Milling experiments were performed using a FlackTek SpeedMixer DAC 330-100 SE purchased from FlackTek Manufacturing. Experiments were conducted in either 5 or 15 mL stainless steel jars with either 7 mm or 10 mm ⌀ stainless steel grinding balls, both obtained from Form-Tech Scientific. A custom holder acquired from Form-Tech Scientific was used to hold the milling jars in the Speedmixer. Experiments were performed at a frequency at 1500 rpm for various times. The Speedmixer was operated for a maximum of 5 minutes with a 30 second rest period required thereafter. For experiments longer than 5 minutes, multiple rounds of milling were performed (e.g., 6 minutes of milling were performed in two rounds of 3 minutes and 20-minute experiments performed as four 5-minute sessions).

2.3 Neutralization of beta blocker salts

All studied beta blockers with the exception of **Ate** required the isolation of the free base form from the commercially purchased HCl (**Pro**, **Ace**, **Lab**) or tartrate (**Met**) salts. This was achieved using milling.

The general procedure involved adding the commercial salt to a 15 mL milling jar together with 1 (**Pro** and **Lab**), 1.5 (**Ace**), or 2 (**Met**) molar equivalent of pre-milled sodium hydroxide pellets. Excess NaOH was used for **Ace** since unsatisfactory yields of 65% or lower were obtained using 1 mole equivalence. 100 μL of distilled water was then added to the mixture together with two 10 mm ⌀ milling balls. This mixture was then milled for 10 minutes at 1500 rpm. For **Pro** and **Met**, the milled material was dissolved in ethyl acetate and the jars washed with water and ethyl acetate. Liquid-liquid extraction was performed, and the ethyl acetate layer dried with anhydrous magnesium sulfate. The solid was filtered off and the remaining solvent removed *in vacuo*. **Pro** was isolated as a white solid while **Met** yielded a colorless oil which, upon cooling, solidified as a white solid. **Ace** and **Lab** were isolated without liquid-liquid extraction. First, the milling jars were washed out with 30 mL of water, which was added to a beaker and stirred at room temperature for 1 hour. Thereafter, white solid of the free base was filtered off and dried. All the free bases were isolated in high yield (**Pro** = 84%, **Met** = 97%, **Ace** = 81%, **Lab** = 90%). Table S3 lists the specific details of these neutralizations.

Table S3: Experimental details of the commercial beta blocker salt neutralizations

Commercial salt				NaOH		H_2O	Free base		
Salt	**MW (g/mol)**	**Mass (g)**	**Moles (mmol)**	**Mass (g)**	**Moles (mmol)**	**η (µL/mg)**	**MW (g/mol)**	**Yield (g)**	**%**
Pro HCl	295.80	1.000	3.381	0.135	3.381	0.0881	259.34	0.738	84
Met tartrate	342.41	2.000	5.841	0.467	11.68	0.0405	267.36	1.565	97
Ace HCl	372.88	1.000	2.682	0.161	4.023	0.0861	336.44	0.734	81
Lab HCl	364.87	1.000	2.741	0.110	2.741	0.0901	328.41	0.811	90

2.4 Crystallizations

2.4.1 Beta blocker free base crystallizations

Preparation of Ace

Single crystals of the free base **Ace** were prepared by slow evaporation of a solution of **Ace** in methanol.

2.4.2 Beta blocker NA and INA salt cocrystallizations

All **NA** and **INA** beta blocker salts were prepared using liquid-assisted grinding (LAG) followed by slow evaporation experiments to yield crystals. 80 mg of beta blocker (as the free base) and 1 mole equivalence of **NA** or **INA** were added to a 5 mL milling jar together with one 7 mm ⌀ milling ball and 30 µL of solvent. After 3 minutes of milling, powder X-ray diffraction (PXRD) was performed on the resulting powders to assess the presence of a new phase. When a new phase was evident, single crystals of the salts were then grown by dissolving the crystalline material prepared from LAG in the solvent used for LAG and allowing the solvent to slowly evaporate. Crystals suitable for X-ray diffraction were obtained within at most 3-4 days. Table S4 details the specific amounts and solvent used.

Table S4: LAG conditions used for the formation of the **beta blocker**·**NA**/**INA** salt crystals

	Beta blocker		NA/INA		
Salt	**Mass (mg)**	**Moles (mmol)**	**Mass (mg)**	**Moles (mmol)**	**Solvent**
Pro·NA	80	0.31	38	0.31	MeCN
Pro·INA	80	0.31	38	0.31	IPA
Met·NA	80	0.30	37	0.30	IPA
Met·INA	80	0.30	37	0.30	MeCN
Ace·NA	80	0.24	29	0.24	MeCN
Ace·INA	80	0.24	29	0.24	MeCN
Ate·NA	80	0.30	37	0.30	MeOH
Ate·INA	80	0.30	37	0.30	MeCN
Lab·NA*					
Lab·INA	80	0.24	30	0.24	MeCN

*No experiments led to successful cocrystallization of **Lab** with **NA**.

2.4.3 Salt generation from slow evaporation and seeding

Once single crystals of each beta blocker salt were grown and phase-pure salts were obtained from LAG, the likelihood of cocrystallization via slow evaporation and seeding was assessed. For both procedures, 50 mg of beta blocker together with 1 equivalence of **NA** or **INA** were dissolved in the solvent used in the successful LAG experiments (see Table S4). For the seeding experiments, a spatula tip of the phase pure crystalline material obtained from LAG was added to the solution and then the solvent was allowed to evaporate. Solid material or oils were obtained, and the solids were analyzed via PXRD.

Table S5: Summary of results from slow evaporation and seeding experiments

	Crystallizations	
Salt	**Slow evaporation**	**Seeding**
Pro·NA	x, oil	✓
Pro·INA	✓	✓
Met·NA	✓	✓
Met·INA	✓	✓
Ace·NA	x, oil	x
Ace·INA	✓	✓
Ate·NA	x, oil	x, oil
Ate·INA	x	✓
Lab·INA	✓	✓

3. Single-crystal X-ray diffraction (SCXRD)

3.1 General collection and refinement details

Reflection Intensity data were collected at 100 K with the use of an Oxford cryostream on either a Rigaku XtaLAB Synergy-i Kappa (Synergy) or a Bruker D8 Venture 3-circle (Venture) diffractometer. The Synergy consisted of a PhotonJet-i X-ray source operating at 50 W (50kV, 1 mA) to generate Cu Kα radiation (λ = 1.54178 Å) and equipped with a HyPix-6000HE HPC detector. The Venture consisted of a microfocus Mo Kα (λ = 0.71073 Å) source also operating at 50 W (50kV, 1 mA) with a Photon 100 CMOS area detector. Crystals were transferred from their crystallization vials and placed on a glass slide in either NVH immersion or paratone oil and an optical microscope was used to select and mount a suitable crystal onto a MiTeGen or Hampton Research Cryoloop. Crystals were centered using a video camera to ensure that no translations were observed as the crystal was rotated during the data collection. Crystals were also measured for size, morphology, and color.

For data collections using the Synergy, the software *CrysAlis*^{Pro} [27] was used. A unit cell determination was carried out and a data collection strategy was undertaken after it was confirmed that the unit cell obtained was not that of one of the coformers. After data collection, the unit cell was re-determined using a subset of the full data collection. Intensity data were corrected for Lorentz, polarization, and background effects. A numerical absorption correction was applied based on a Gaussian integration over a multifaceted crystal and followed by a semi-empirical correction for adsorption applied using the program *SCALE3 ABSPACK*.[28] Collections on the Venture involved using the APEX4[29] software together with SAINT[30] for cell refinement and data reduction, SADABS[30] for absorption corrections and XPREP[30] for the space group determinations.

Crystal structures were solved by intrinsic phasing using SHELXT[31] within the Olex2[32] GUI. Non-hydrogen atoms were first refined isotropically followed by anisotropic refinement by full matrix least-squares calculations based on F^2 using SHELXL-2018.[33, 34] SHELXL-2018 restraints were used during the refinements as required. Hydrogen atoms bound to oxygen and nitrogen atoms were located in the difference Fourier map and allowed to refine freely where possible while hydrogens bound to carbon atoms were geometrically constrained using the appropriate AFIX commands. Platon[35] was used to validate CIF files while Mercury[36] and BIOVIA Discovery Studio[37] were used for generating molecular graphics and crystal structure analysis.

3.2 Structure specific refinement details

Ace refinement details
The alkanolamine chain (C14-C18) was disordered over two positions in a 74:26 ratio. SIMU restraints were used on the overlapping oxygens to maintain reasonable ADPs.

Ace·INA refinement details
One of the **Ace** molecules exhibits minor disorder of the alkanolamine alcohol carbon (C14). This minor component (C14A) was modelled isotropically with the occupancy fixed at 10%. SADI restraints were applied to the bond lengths of both components. The hydrogen on O4 for the minor component was not modelled as the C-O-H angle is unrealistic.

Ate·NA refinement details

Ate·NA crystallized together with methanol. The methanol was disordered over two positions in a 57:43 ratio with SIMU restraints used to maintain reasonable ADPs. DFIX restraints of 1.43 Å were also used on the C-O bond lengths while the alcohol hydrogens were geometrically placed with AFIX 147 commands.

Lab·INA refinement details

The pharmaceutical component is a mixture of four stereoisomers, resulting in the hydroxyl group (O3) being disordered over two positions on the chiral center (C8). The hydroxyl groups were constrained to an occupancy of 0.50. The phenyl ring (C14>C19) was also disordered over two positions. The ring was split into parts A and B and allowed to freely refine. SIMU, RIGU, and AFIX 66 restraints were used on both parts to maintain reasonable bond lengths and ADPs. The occupancy for part A was 60%, and 40% for part B. The aromatic ring of isonicotinic acid was also disordered over two positions. The ring was split into parts A and B and allowed to freely refine. SIMU, RIGU, and FLAT restraints were used to maintain reasonable geometries and ADPs. The occupancy of part A was 39% and part B 61%.

3.3 Data table

(next page)

Table S6: Crystallographic data for all the crystal structures reported

Name	Pro·NA	Pro·INA	Met·NA	Met·INA	Ace free base	Ace·NA	Ace·INA	Ate·NA	Ate·INA	Lab·INA
Chemical Formula	$C_{22}H_{26}N_2O_4$	$C_{22}H_{26}N_2O_4$	$C_{21}H_{30}N_2O_5$	$C_{21}H_{30}N_2O_5$	$C_{18}H_{28}N_2O_4$	$C_{24}H_{33}N_3O_6$	$C_{24}H_{33}N_3O_6$	$C_{21}H_{31}N_3O_6$	$C_{22}H_{30}N_4O_5$	$C_{25}H_{29}N_3O_5$
Formula Mass	382.45	382.45	390.47	390.47	336.42	459.53	459.53	421.49	430.50	451.51
Crystal System	Monoclinic	Triclinic	Triclinic	Triclinic	Triclinic	Triclinic	Triclinic	Triclinic	Monoclinic	Triclinic
Space Group	$P2_1/c$	P-1	P-1	P-1	P-1	P-1	P-1	P-1	$P2_1/c$	P-1
a/Å	15.3968(3)	8.0313(2)	8.08110(10)	7.75330(10)	5.2863(2)	11.1288(2)	11.2068(2)	7.5713(2)	18.4840(2)	7.8447(3)
b/Å	8.65850(10)	10.0546(2)	9.22040(10)	8.87140(10)	12.5574(5)	13.1402(2)	13.1295(2)	9.0568(3)	14.6742(2)	12.5695(6)
c/Å	16.3567(3)	13.9004(3)	14.2988(2)	16.1407(2)	14.3948(5)	25.5766(2)	25.6226(4)	16.9380(5)	8.34950(10)	12.6336(5)
α/°	90	70.899(2)	99.0000(10)	86.5820(10)	68.479(4)	76.0570(10)	75.5690(10)	77.3660(10)	90	76.247(4)
β/°	109.839(2)	74.871(2)	93.9190(10)	78.5720(10)	80.815(3)	82.4310(10)	81.5610(10)	88.6140(10)	90.1200(10)	77.590(3)
γ/°	90	76.988(2)	98.5330(10)	78.7090(10)	86.522(3)	77.3610(10)	75.4320(10)	76.5550(10)	90	85.371(3)
V/Å^3	2051.15(6)	1011.83(4)	1036.07(2)	1066.88(2)	877.54(6)	3529.68(9)	3519.52(10)	1101.85(6)	2264.70(5)	1181.16(9)
ρ_{calc}/g cm^{-3}	1.238	1.255	1.252	1.215	1.273	1.297	1.301	1.270	1.263	1.270
T/K	100.00(10)	100.01(10)	100.15	100.15	100.02(13)	100.00(15)	100.0(2)	100.00	100.00(10)	100.15
Z	4	2	2	2	2	6	6	2	4	2
Radiation type	Cu Kα	Cu Kα	Cu Kα	Cu Kα	Cu Kα	Cu Kα	Cu Kα	Mo Kα	Cu Kα	Cu Kα
Absorption coefficient, μ/mm^{-1}	0.694	0.703	0.728	0.707	0.729	0.769	0.771	0.093	0.743	0.729
Crystal size/mm	0.151 × 0.081 × 0.05	0.115 × 0.086 × 0.041	0.181 × 0.138 × 0.06	0.275 × 0.146 × 0.109	0.13 × 0.05 × 0.03	0.12 × 0.08 × 0.06	0.179 × 0.061 × 0.043	0.232 x 0.112 x 0.094	0.175 × 0.059 × 0.043	0.13 × 0.125 × 0.064
No. of reflections measured	27202	21381	33458	52647	13752	106207	96708	35708	31464	33944
No. of independent reflections	4208	4079	4334	4484	3623	15222	14782	5440	4594	4927
No. of reflections ($I>2\sigma(I)$)	3592	3253	3968	4202	3330	13634	12962	4259	3937	3890
R_{int}	0.0601	0.0465	0.0284	0.0415	0.0351	0.0488	0.0468	0.0481	0.0509	0.0554
Final R_1 ($I>2\sigma(I)$)	0.0476	0.0420	0.0398	0.0353	0.0792	0.0467	0.0646	0.0610	0.0394	0.0559
Final $wR(F^2)$ ($I>2\sigma(I)$)	0.1191	0.1014	0.1048	0.0895	0.1728	0.1247	0.1662	0.1250	0.0981	0.1402
Final R_1 (all data)	0.0574	0.0556	0.0428	0.0372	0.0850	0.0519	0.0733	0.0842	0.0475	0.0706
Final $wR(F^2)$ (all data)	0.1248	0.1077	0.1072	0.0909	0.1760	0.1292	0.1734	0.1388	0.1031	0.1489
Goodness-of-fit on F^2	1.024	1.065	1.039	1.053	1.186	1.071	1.090	1.056	1.036	1.062
CCDC deposition no.	2371670	2371671	2371672	2371673	2371674	2371675	2371676	2371677	2371678	2371679

4. Single crystal X-ray structures

4.1 X-ray structures showing thermal ellipsoids

For all the figures below, carbon, hydrogen, oxygen and nitrogen atoms are represented by gray, white, red, and light blue ellipsoids, respectively and thermal ellipsoids are plotted at 50% probability.

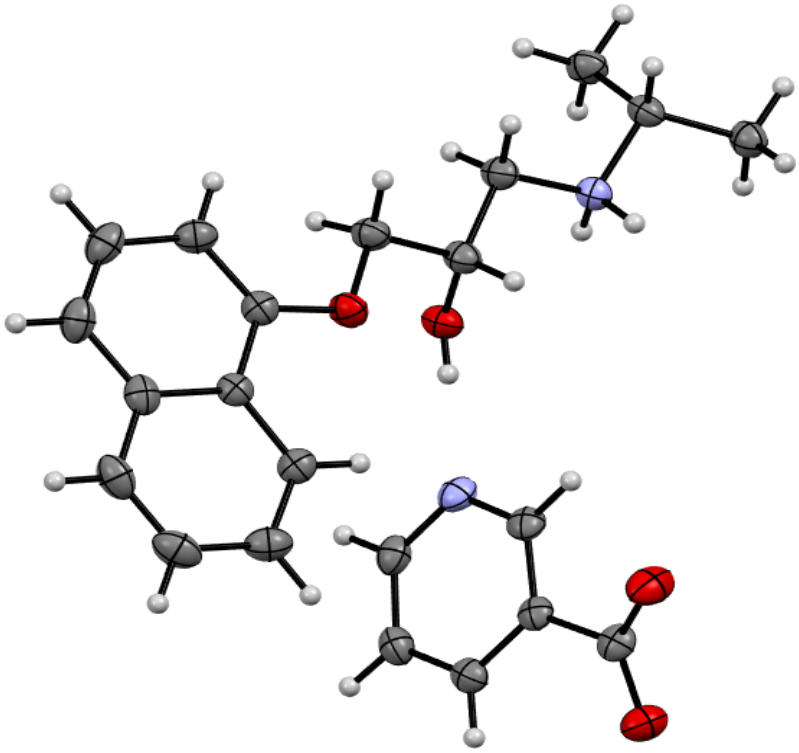

Figure S1. Asymmetric unit of **Pro·NA**.

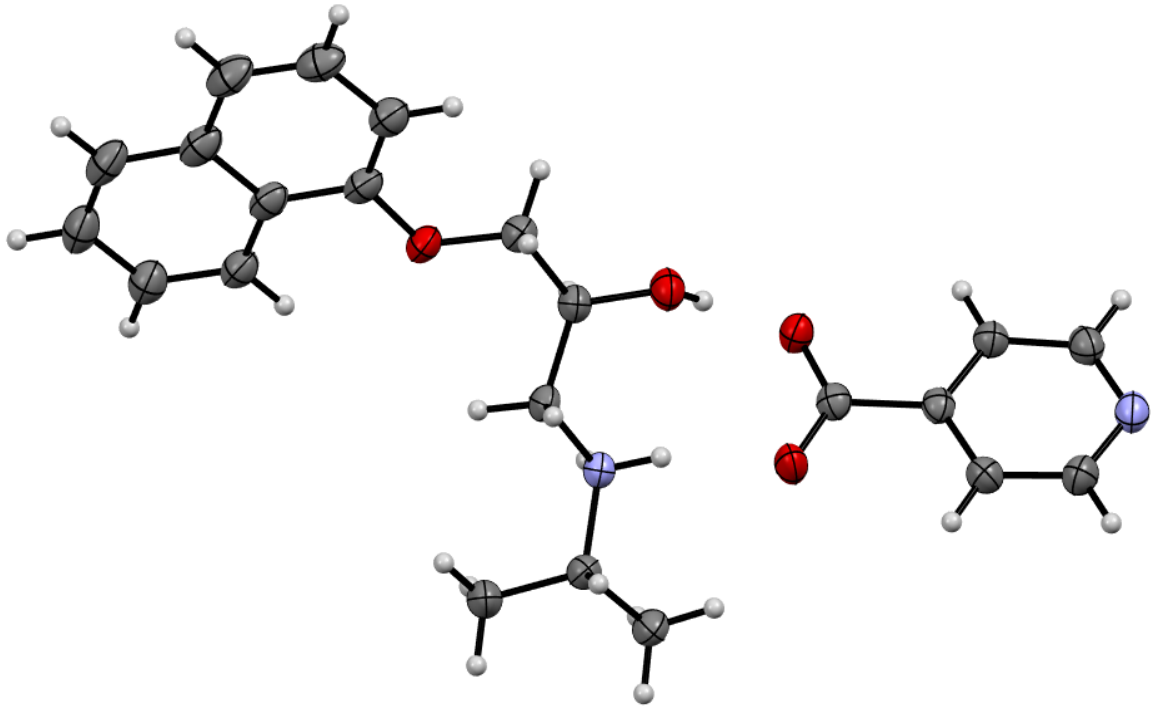

Figure S2. Asymmetric unit of **Pro·INA**.

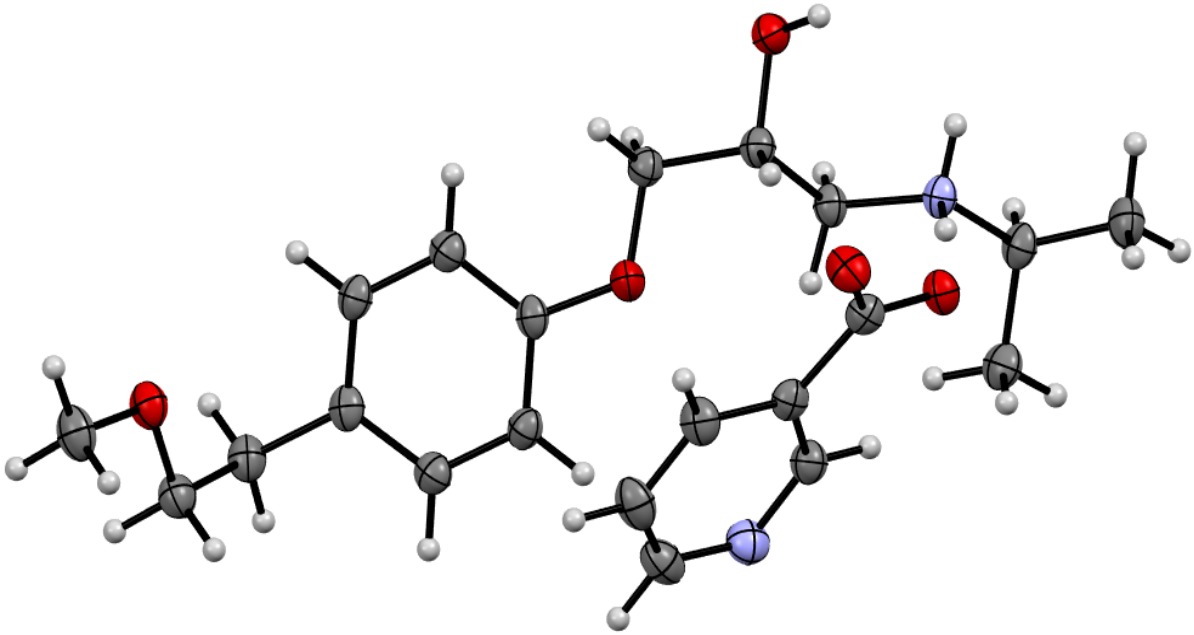

Figure S3. Asymmetric unit of **Met·NA**.

Figure S4. Asymmetric unit of **Met·INA**.

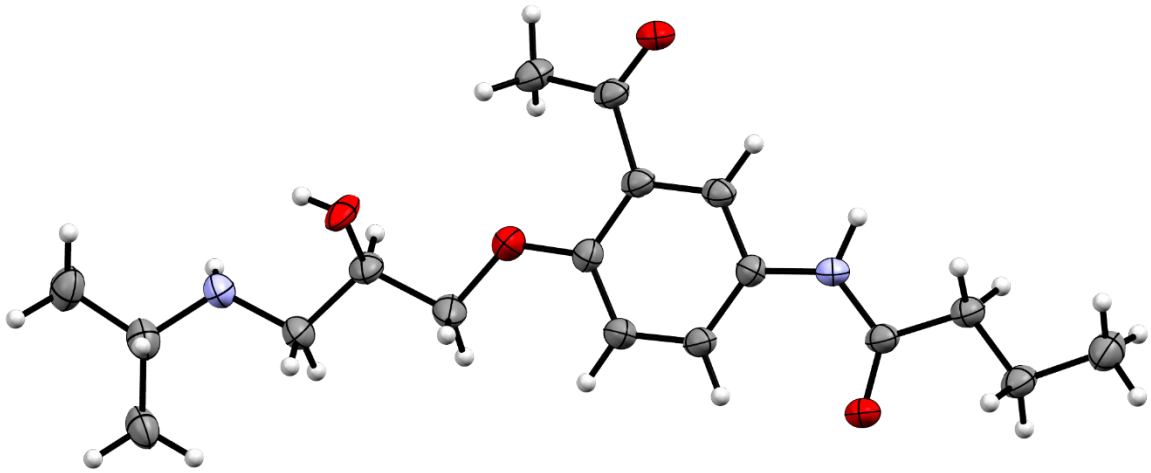

Figure S5. Asymmetric unit of **Ace** (free base) with disorder removed for clarity.

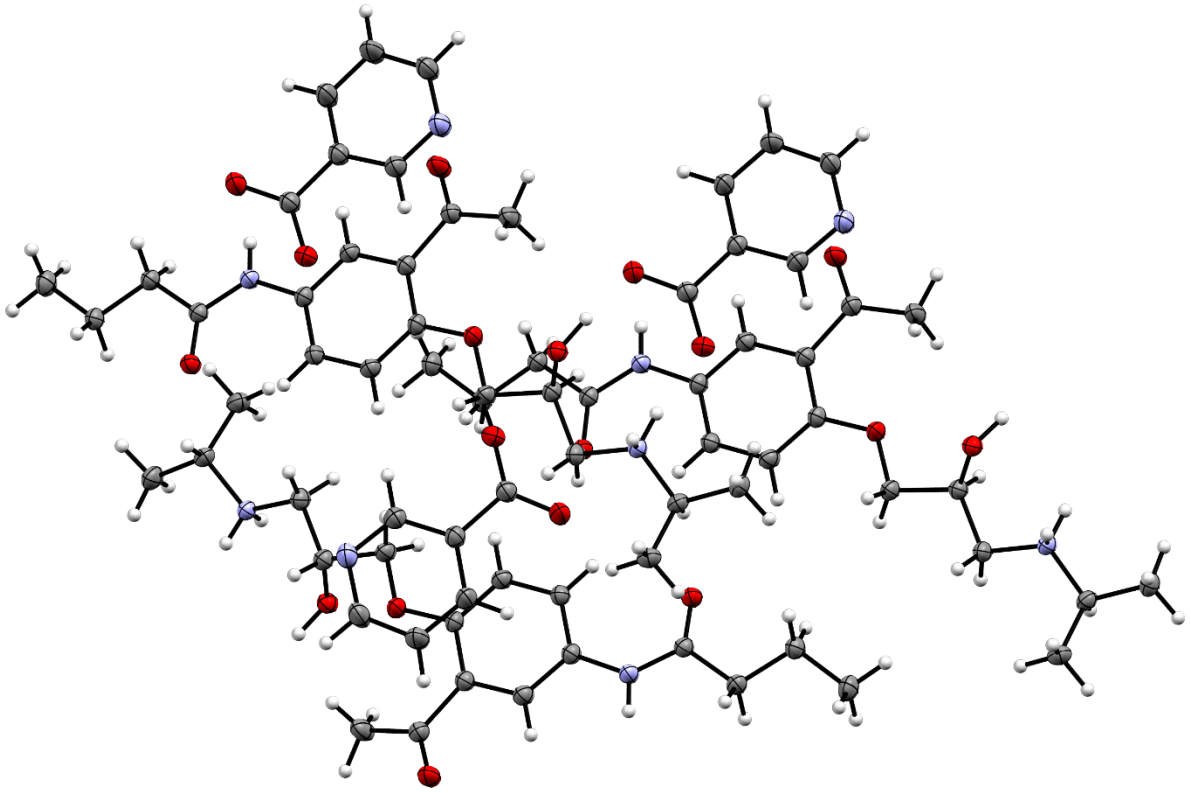

Figure S6. Asymmetric unit of **Ace·NA**.

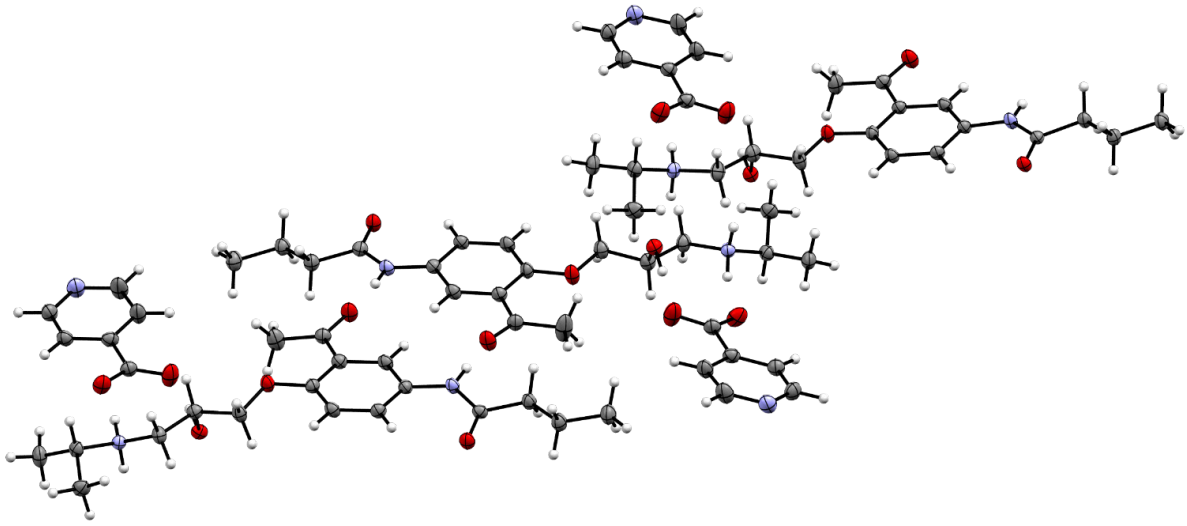

Figure S7. Asymmetric unit of **Ace·INA** with disorder removed for clarity.

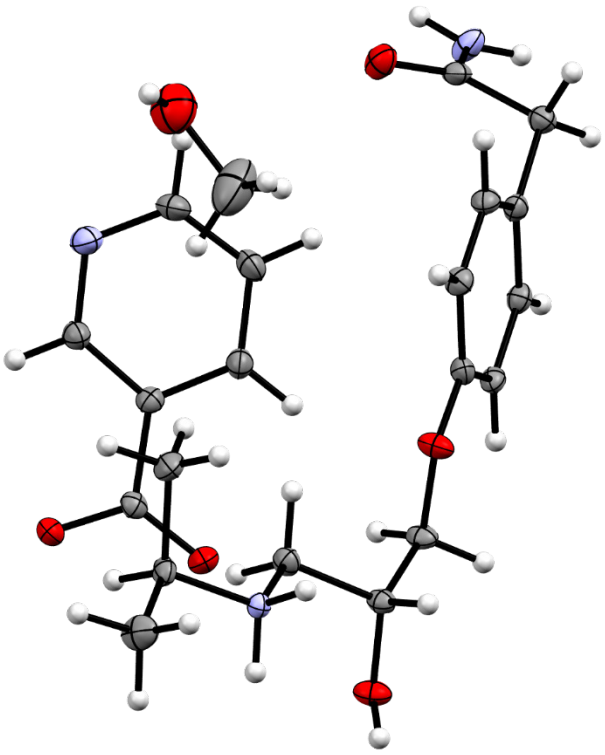

Figure S8. Asymmetric unit of **Ate·NA** with disorder of the MeOH removed for clarity.

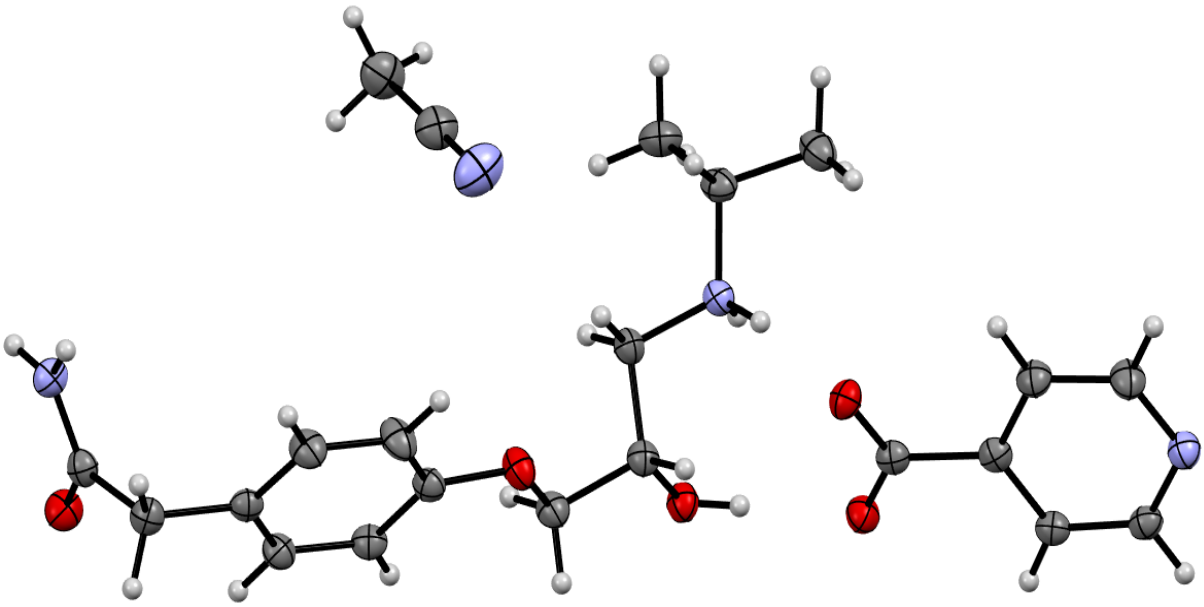

Figure S9. Asymmetric unit of **Ate·INA**.

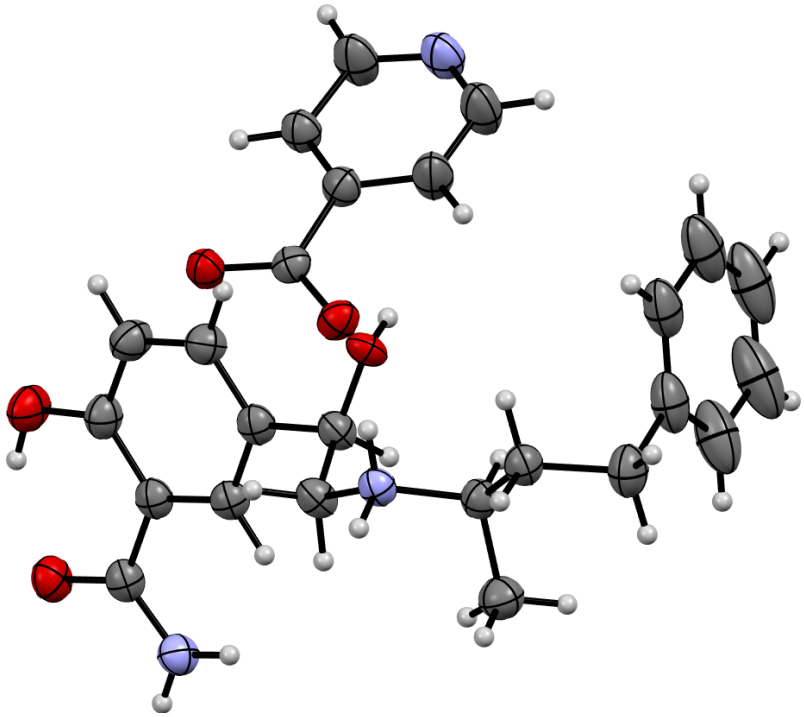

Figure S10. Asymmetric unit of **Lab·INA** with disorder removed for clarity.

4.2 Structural descriptions and additional figures

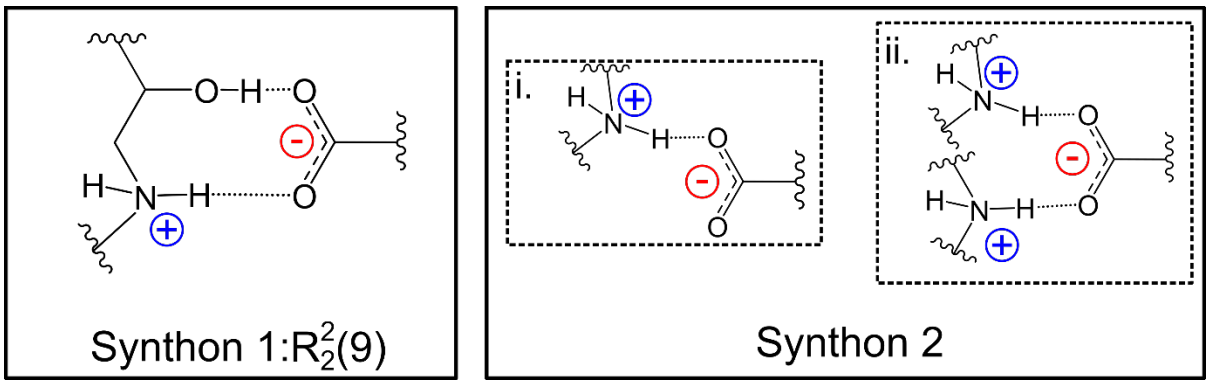

Figure S11. The two charge-assisted hydrogen bonding synthons commonly observed in the **beta blocker·NA/INA** salts. Synthon 2 was observed in two variations; the carboxylate either interacts with one distinct protonated amine (i), which is present together with synthon 1 or the carboxylate interacts with two distinct protonated amines (ii).

<u>Pro structures</u>:

Pro·NA crystallized in the space group $P2_1/c$ with the carboxylate of **NA** interacting with two charged amines on different **Pro** molecules (Figure S11: synthon 2ii) [O···N separations: 2.767(2) Å (O4···N1), 2.850(2) Å (O3···N1) and 3.012(2) Å (O4···N1)]. The pyridine nitrogen further interacts via hydrogen bonding with the alcohol on **Pro**

[N1···O1 separation: 2.776(2) Å]. Together, one carboxylate-amine (from synthon 2ii) and the pyridine-alcohol hydrogen bonds result in formation of a large hydrogen-bonded ring involving two **Pro** molecules and two **NA** molecules with graph set $R_4^4(22)$ (Figure S12). These rings are linked into an infinite chain through the second carboxylate-amine hydrogen bond (from synthon 2ii).

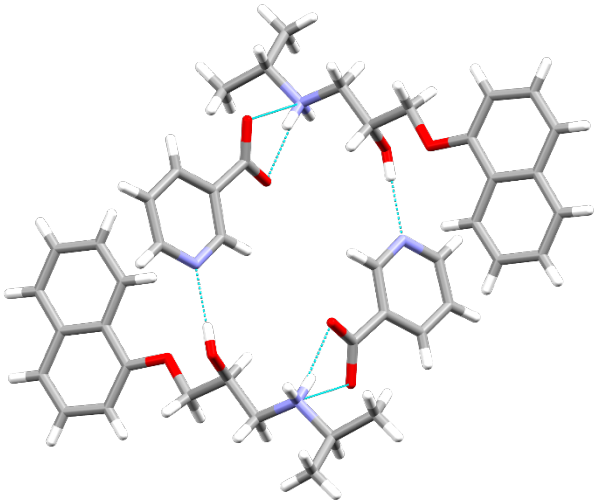

Figure S12. $R_4^4(22)$ hydrogen-bonded ring in **Pro·NA** comprised of two **Pro** and two **NA** molecules.

Pro·INA crystallized in the space group *P*-1. The carboxylate of **INA** interacts via synthon 1 and synthon 2i (Figure S11) [O···N separations: 2.758(2) Å (O3···N1) and 2.793(2) Å (O4···N1] and O3···O4 separation: 2.681(1) Å]. Together, synthon 1 and 2i assemble two molecules of **Pro** and two molecules of **INA** into a supramolecular ring held together by six hydrogen bonds (Figure S13). The pyridine does not participate in hydrogen bonding and instead exhibits weak N···H-C hydrogen bonding [N2···C2 separation: 3.528(3) Å]. Given the lack of any additional strong hydrogen-bond donors, neighboring supramolecular rings interact through weaker C-H···O and C-H···π contacts.

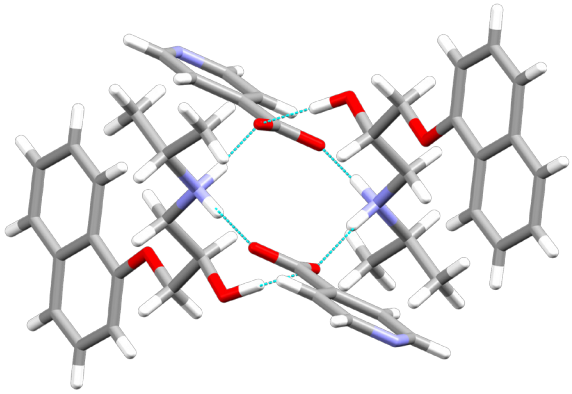

Figure S13. Supramolecular ring observed in **Pro·INA** consisting of two **Pro** and two **INA** molecules held together through six hydrogen bonds.

Met structures:

Met·NA formed in the space group *P*-1 with the carboxylate of **NA** engaging in synthons 1 and 2i (Figure S11) [O···N separations: 2.797(1) Å (O4···N1), 2.751(1) Å (O5···N1); O4···O3 separation: 2.707(1) Å]. Similar to other solids above, synthon 1 and 2i assemble two molecules of **Met** and two molecules of **NA** into a supramolecular ring held together by six hydrogen bonds. The pyridine of **NA** is not involved in any strong hydrogen bonding but rather weaker N···H-C interactions with the aromatic ring and the ether side chain of **Met** [N···C separations: 3.498(2) Å (N2···C9), 3.591(2) Å (N2···C3)]. Given the lack of any additional strong hydrogen-bond donors, neighboring supramolecular rings interact through weaker C-H···O and C-H···π contacts (similar to **Pro·INA**).

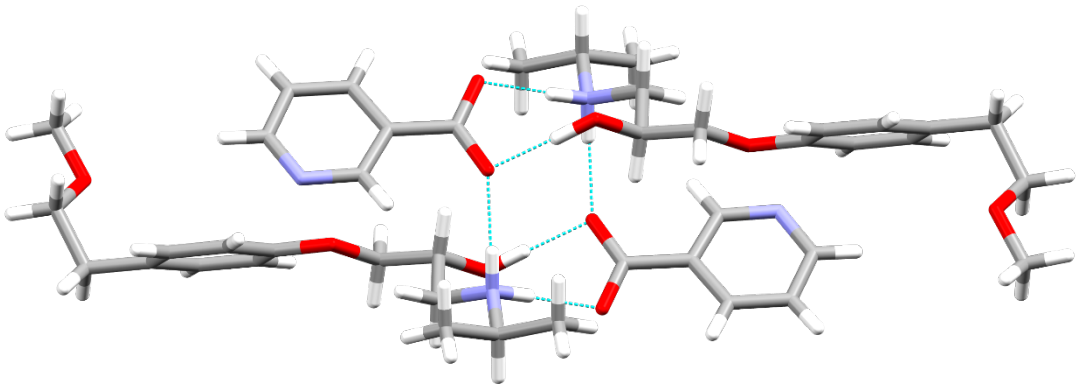

Figure S14. Supramolecular ring observed in **Met·NA** consisting of two **Met** and two **NA** molecules linked via six hydrogen bonds.

Met·INA also crystallized in the *P*-1 space group with the carboxylate of **INA** forming synthons 1 and 2i with **Met** molecules (Figure S11) [O···N separations: 2.762(1) Å (O4···N1), 2.789(1) Å (O5···N1); O5···O3 separation: 2.695(1) Å]. Akin to **Met·NA**, the components of **Met·INA** self-assemble into a supramolecular ring involving two molecules of **Met** and two molecules of **INA** held together by six hydrogen bonds. The pyridine rings of **INA** also do not exhibit strong interactions and show weaker N···H-C

interactions with the aromatic ring of **Met**. The neighboring supramolecular rings also interact through weaker C-H···O and C-H···π contacts.

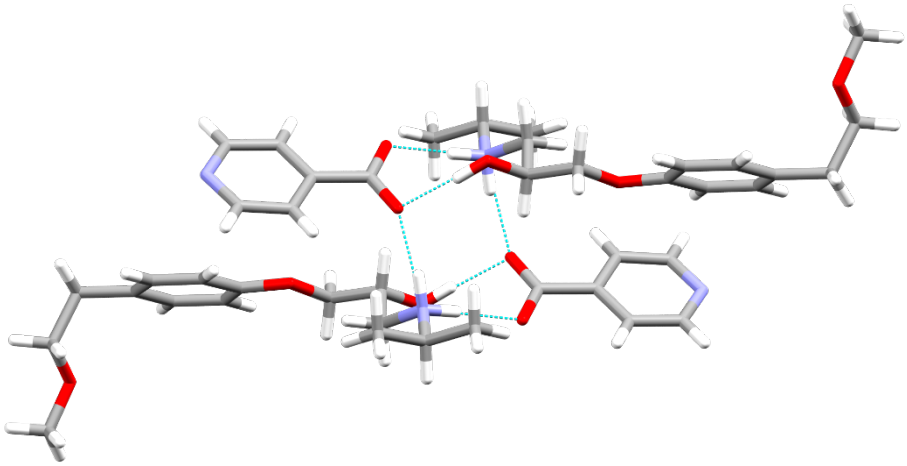

Figure S15. Supramolecular ring observed in **Met·INA** consisting of two **Met** and two **INA** molecules linked via six hydrogen bonds.

Ace structures:

The free base, **Ace**, crystallizes in the space group *P*-1. One molecule of **Ace** is present in the asymmetric unit and the alkanolamine chain is disordered over two positions.

In the major orientation **Ace** molecule, the amine group engages in hydrogen bonding with an alcohol of an adjacent **Ace** [N2···O4 separation: 3.551 Å]. The alcohol also interacts with an adjacent **Ace** alcohol [O4···O4 separation: 2.8913 Å]. In the minor orientation **Ace** molecule, the amine and alcohol engage in hydrogen bonds with adjacent alkanolamine groups on two neighboring **Ace** molecules [N2A···O4A separation: 2.4285 Å, N2A···N2A separation 3.0237 Å] while the alcohol group also engages in hydrogen bonds with amine groups on two neighboring **Ace** molecules [O4A···N2A separations: 2.4285 Å, 3.1463 Å].

The hydrogen bonds involving the amine and alcohol self-assemble **Ace** molecules into an infinite hydrogen-bonded chain. Akin to the salt structures, the ketone and amide on **Ace** interact with the ketone and amide of a neighboring **Ace** to form a hydrogen-bonded dimer with graph set $R_2^2(14)$ [O2···N1 separation: 2.9219 Å]. These dimers serve to connect the hydrogen-bonded chains.

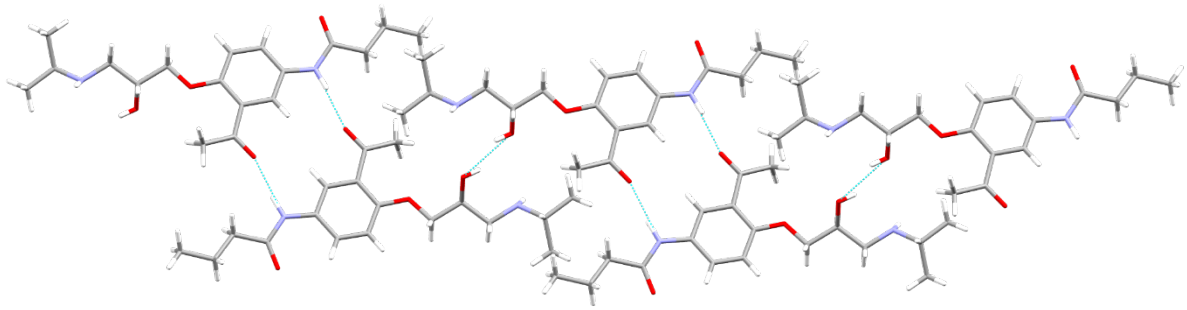

Figure S16. Hydrogen-bonded chains in **Ace**.

Both **Ace·NA** and **Ace·INA** crystallize in the space group *P*-1 and consist of three pairs of molecules in their respective asymmetric units (see Figure S6-S7). In **Ace·NA**, the carboxylates all interact with the charged amine and alcohol on **Ace** (Figure S11: synthon 1) [O···N separations: 2.685(2) Å (O13···N6), 2.692(2) Å (O15···N4), 2.694(2) Å (O18···N2); O···O separations: 2.504(1) Å (O14···O12), 2.513(1) Å (O16···O8), 2.494(1) Å (O17···O4)]. The alkanolamine group on the **Ace** molecule further engages in N^+···H-O hydrogen-bonded dimers with the alkanolamine group on an adjacent **Ace** molecule forming a graph set of $R_2^2(10)$ [N···O separations: 2.731(1) Å (N4···O4), 2.765(1) Å (N2···O8), 2.754(1) Å (N6···O12)] (Figure S17). Overall, the combination of synthon 1 and the alkanolamine dimer forms a large, supramolecular hydrogen-bonded ring.

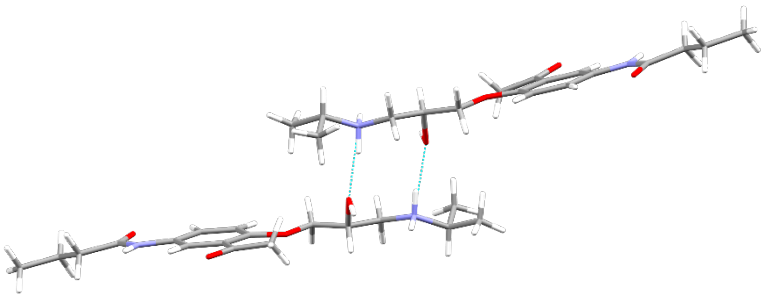

Figure S17. $R_2^2(10)$ hydrogen-bonded dimers between adjacent **Ace** molecules in **Ace·NA**.

The pyridines of **NA** form dimers with other **NA** molecules through weak N···H-C bonding. Furthermore, the ketone and amide on **Ace** also interact with the ketone and amide of a neighboring **Ace** to form a hydrogen-bonded dimer with graph set $R_2^2(14)$ [O···N separation: 2.903(2) Å (O2···N5), 2.919(2) Å (O6···N3), 2.971(2) Å (O10···N1)]. The amide of **Ace** also interacts via weak O···H-C interactions with its neighboring **Ace** and, overall, these hydrogen bonds between **Ace** molecules form a hydrogen-bonded sheet, with **NA** molecules lying at the edges (Figure S18).

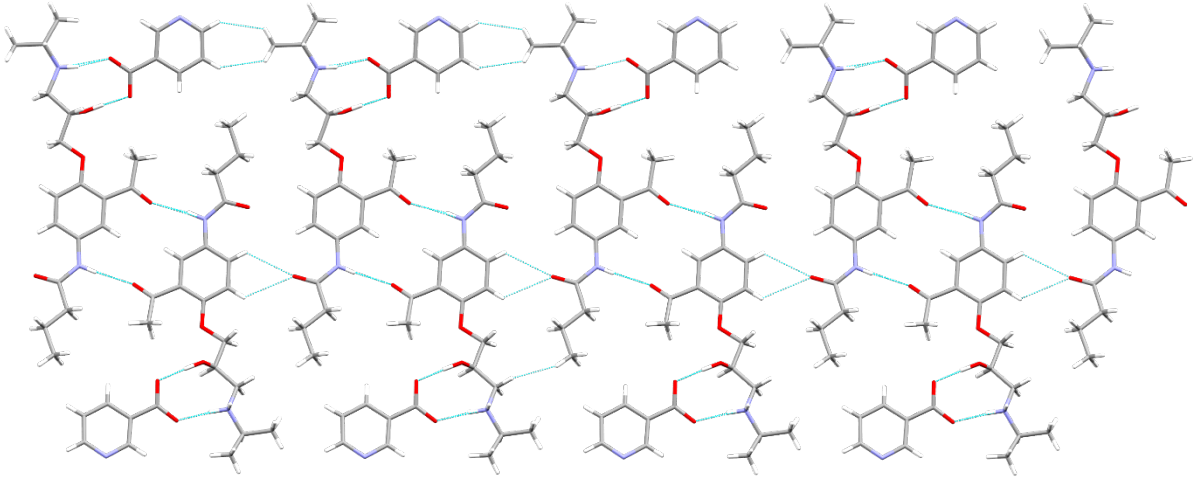

Figure S18. Hydrogen-bonded sheet observed in **Ace·NA**.

Ace·INA displays very similar interactions and packing characteristics as **Ace·NA** and they are isostructural. The carboxylates of **INA** all interact with the charged amine and alcohol of **Ace** (Figure S11: synthon 1) [O···N separations: 2.695(4) Å (O6···N2), 2.731(4) Å (O12···N5), 2.709(4) Å (O18···N8); O···O separations: 2.502(3) Å (O5···O4), 2.486(3) Å (O11···O10), 2.507(3) Å (O17···O16)]. The alkanolamine group on the **Ace** molecule further engages in N^+···H-O hydrogen-bonded dimers with the alkanolamine group on an adjacent **Ace** molecule with graph set $R_2^2(10)$ [N···O separations: 2.744(4) Å (N2···O4), 2.772(4) Å (N5···O16), 2.730(4) Å (N8···O10)]. The pyridines of **INA** also form dimers with other **INA** molecules via weak N···H-C bonding. The ketone-amide hydrogen-bonded dimer interactions are also present with graph set $R_2^2(14)$ [O···N separation: 2.929(4) Å (O7···N1), 2.949(4) Å (O13···N7), 2.988(5) Å (O1···N4)]. Overall, the hydrogen bonds between **Ace** molecules form a hydrogen-bonded sheet, with **INA** molecules lying at the edges similar to **Ace·NA**.

<u>Ate structures</u>:

Ate·NA crystallized in the space group *P*-1 as a salt-solvate with methanol. The main interactions present include the carboxylate interacting through synthon 1 and 2i (Figure S11) [O···N separations: 2.763(2) Å (O4···N2) and 2.783(2) Å (O5···N2) and O3···O5 separation: 2.679(2) Å]. Together, synthon 1 and 2i assemble two molecules of **Ate** and two molecules of **NA** into a supramolecular ring held together by six hydrogen bonds (Figure S19).

The pyridine groups are located on the periphery of the supramolecular ring and accept a hydrogen bond from the amide of an adjacent **Ate** molecule [N1···N3 separation: 2.986(2) Å]. The amide engages in a dimer with another adjacent **Ate** molecule [separation: 2.942(2) Å]. The methanol molecules lie on both sides of the dimer and donate a hydrogen bond to the carbonyl of each amide. The hydrogen bonds involving the pyridine, amide, and methanol serve to link the supramolecular rings.

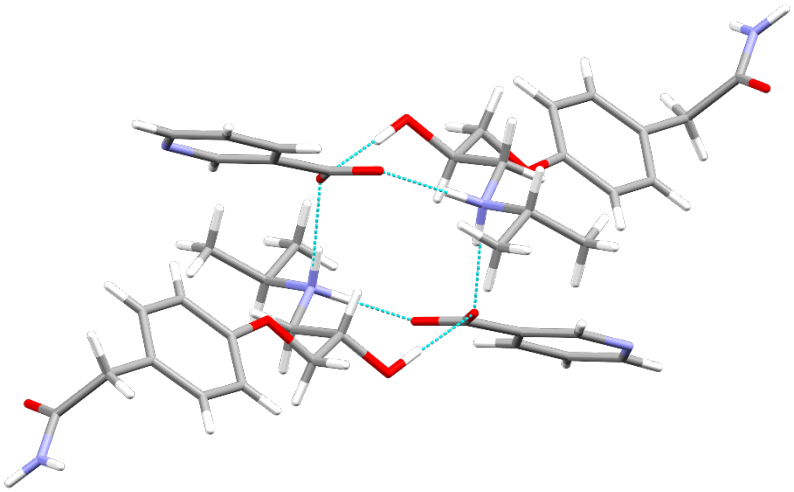

Figure S19. Hydrogen bonding in **Ate·NA** illustrating the supramolecular ring formed by the six hydrogen bonds present between two molecules of both **Ate** and **NA**.

Ate·INA formed in the space group $P2_1/c$ as a salt solvate with an acetonitrile molecule in the asymmetric unit. The carboxylate of **INA** forms synthon 1 and 2i (Figure S11) [O5···N2 separations: 2.774(1) Å and 2.822(1) Å and O4···O3 separation: 2.709(1) Å]. Synthon 1 and 2i assemble the components into an infinite hydrogen bonded chain. The chain is further supported through the amide groups of **Ate**, which interact through only one N–H···O hydrogen bond [N1···O3 separation: 2.941(1) Å] to form a parallel hydrogen-bonded chain (Figure S20). The second N-H of the amide forms a hydrogen bond with the pyridine ring of **INA** [N1···N3 separation: 3.066(2) Å].

The hydrogen bond between the pyridine and amide involves the hydrogen that is *syn* to the carbonyl of the **Ate** molecule rather than the hydrogen that is *anti* to the carbonyl of **Ate**, which is seen in **Ate·NA**. Overall, the alkanolamine, pyridine, and amide hydrogen bonds self-assemble the components into a 2D hydrogen-bonded sheet. It is noteworthy that the acetonitrile molecule does not participate in strong hydrogen bonding and lies between the sheets.

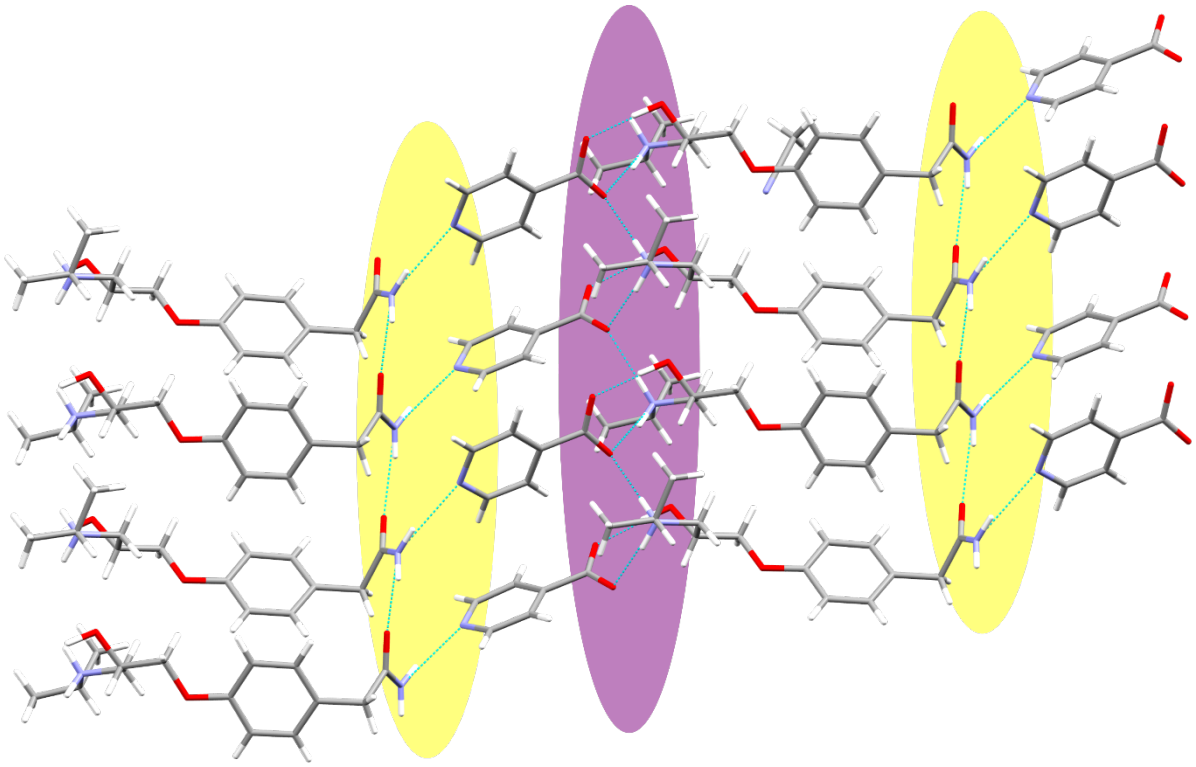

Figure S20. The two types of hydrogen bond chains formed in **Ate·INA**. The center hydrogen bonding chain highlighted in purple is created by the carboxylate and alkanolamine interactions while the chains on the sides highlighted in yellow are formed via pyridine···amide interactions.

Lab structure:

Lab·INA crystallizes in the space group *P*-1 with one pair of the salt present in the asymmetric unit and both molecules exhibit disorder. The carboxylate of **INA** interacts with two charged amines on different **Lab** molecules (Figure S11, synthon 2ii) [O···N separations: 2.740(2) Å (O4···N2) and 2.854(2) Å (O5···N2)]. The synthon 2ii hydrogen bonds assemble two molecules of **Lab** and two molecules of **INA** into a supramolecular hydrogen-bonded ring with graph set $R_4^4(12)$ (Figure S21).

The pyridine nitrogen of **INA** forms a hydrogen bond with the alcohol of an adjacent **Lab** [N···O separations: 2.711(7) Å, 2.92(1) Å, 2.77(1) Å, 2.96(1) Å (disordered N3 and O3)] to connect adjacent rings into an infinite hydrogen-bonded chain. One oxygen of the carboxylate of **INA** (O5) also accepts a hydrogen bond from the amide of an adjacent **Lab** molecule [O···N separation: 2.951(2) Å (O5···N1)]. The amide further engages in a dimer with another adjacent **Lab** molecule and the phenol forms an intramolecular hydrogen bond to the carbonyl of the amide. Overall, the components of **Lab·INA** self-assemble into a 3D hydrogen-bonded network.

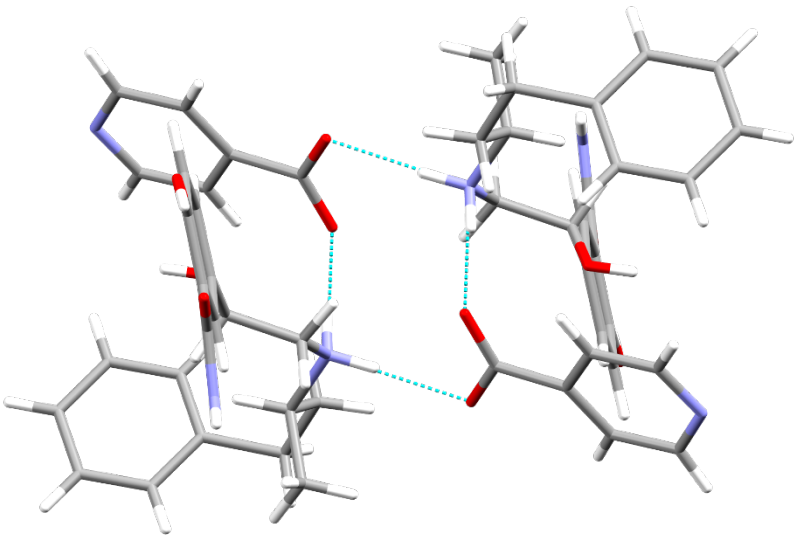

Figure S21. $R_4^4(12)$ hydrogen-bonded ring formed between two **Lab** and two **INA** molecules in **Lab·INA**. Disorder removed for clarity.

5. Powder X-ray diffraction (PXRD)

PXRD patterns were collected on a Rigaku MiniFlex II or Miniflex 6G benchtop powder diffractometer. The X-ray diffraction pattern was obtained by scanning a 2θ range of 3-60°, step size = 0.02°, and scan time of 5 degrees/min. The X-ray source was CuKα radiation (λ =1.5418 Å) with an anode voltage of 30 kV and a current of 15 mA (Miniflex II) or 40 kV and 15 mA (Miniflex 6G) with Bragg-Brentano beam geometry. Diffraction intensities were recorded on a D/teX Ultra position sensitive detector and samples were prepared on zero background holders. Simulated powder patterns derived from crystal structures were generated using Mercury[36] and published structures were obtained from the Cambridge Structural Database (CSD) (PROPRA10,[2] XITNIA[10]) or Crystallography Open Database (COD) (NaCl: 1000041,[38] sodium tartrate: 2223574[39]).

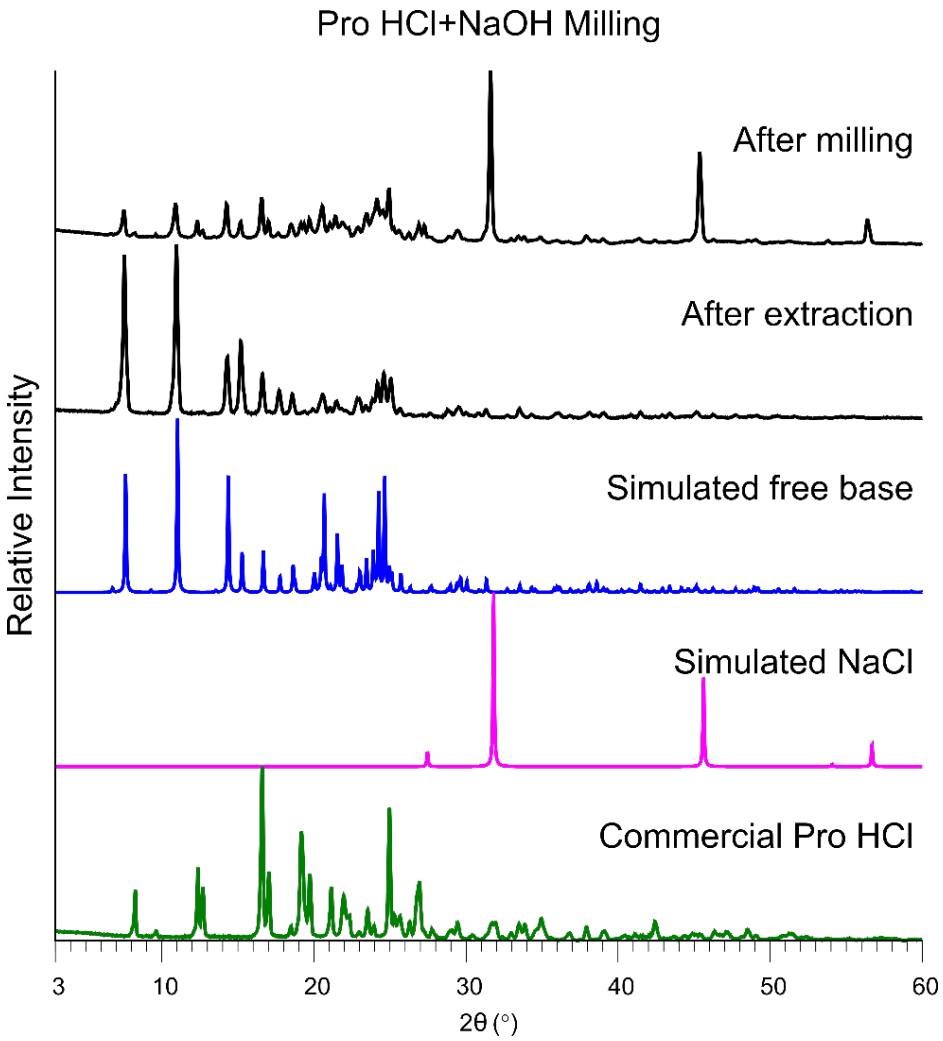

Figure S22. PXRD patterns of the commercial **Pro HCl** milling outcomes. Simulated patterns: Free base PROPRA10[2] (CSD), NaCl 1000041[38] (COD).

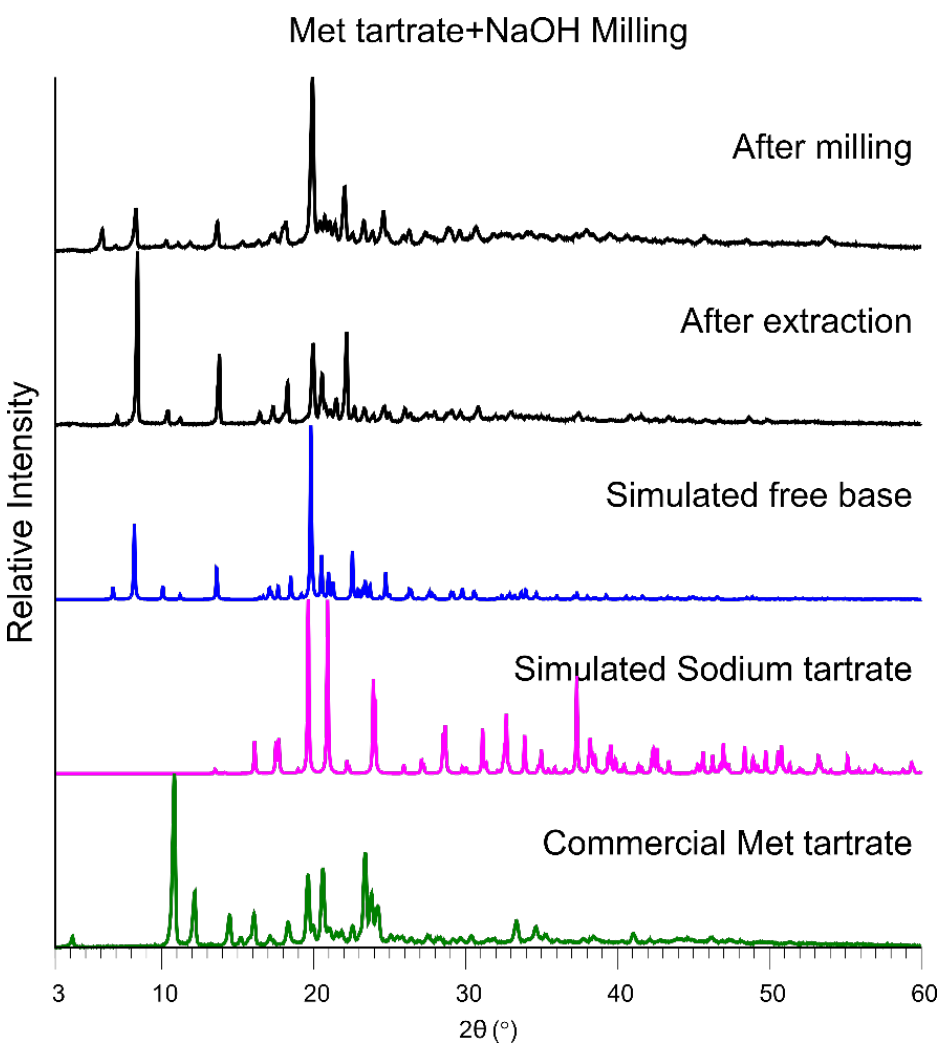

Figure S23. PXRD patterns of the commercial **Met tartrate** milling outcomes. Simulated patterns: Free base XITNIA[10] (CSD), Sodium tartrate 2223574[39] (COD).

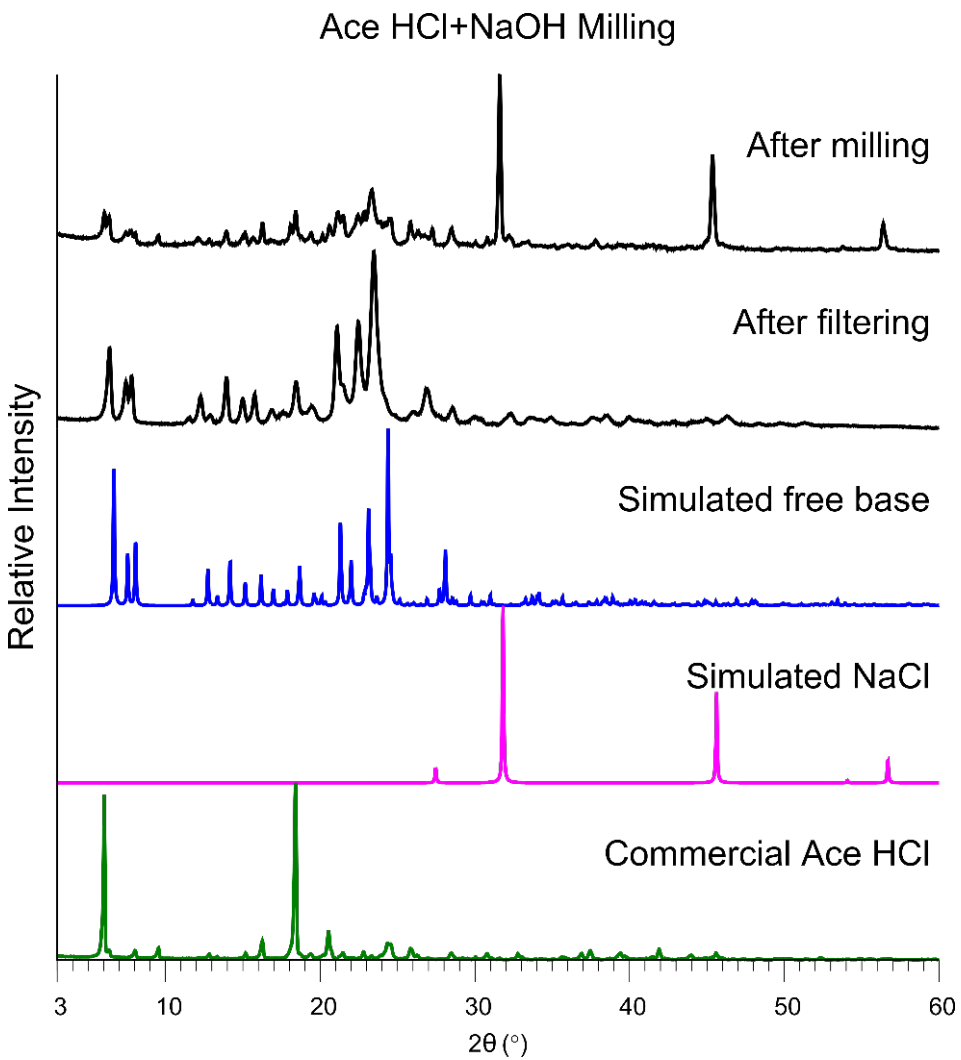

Figure S24. PXRD patterns of the commercial **Ace HCl** milling outcomes. Simulated pattern: NaCl 1000041 (COD).

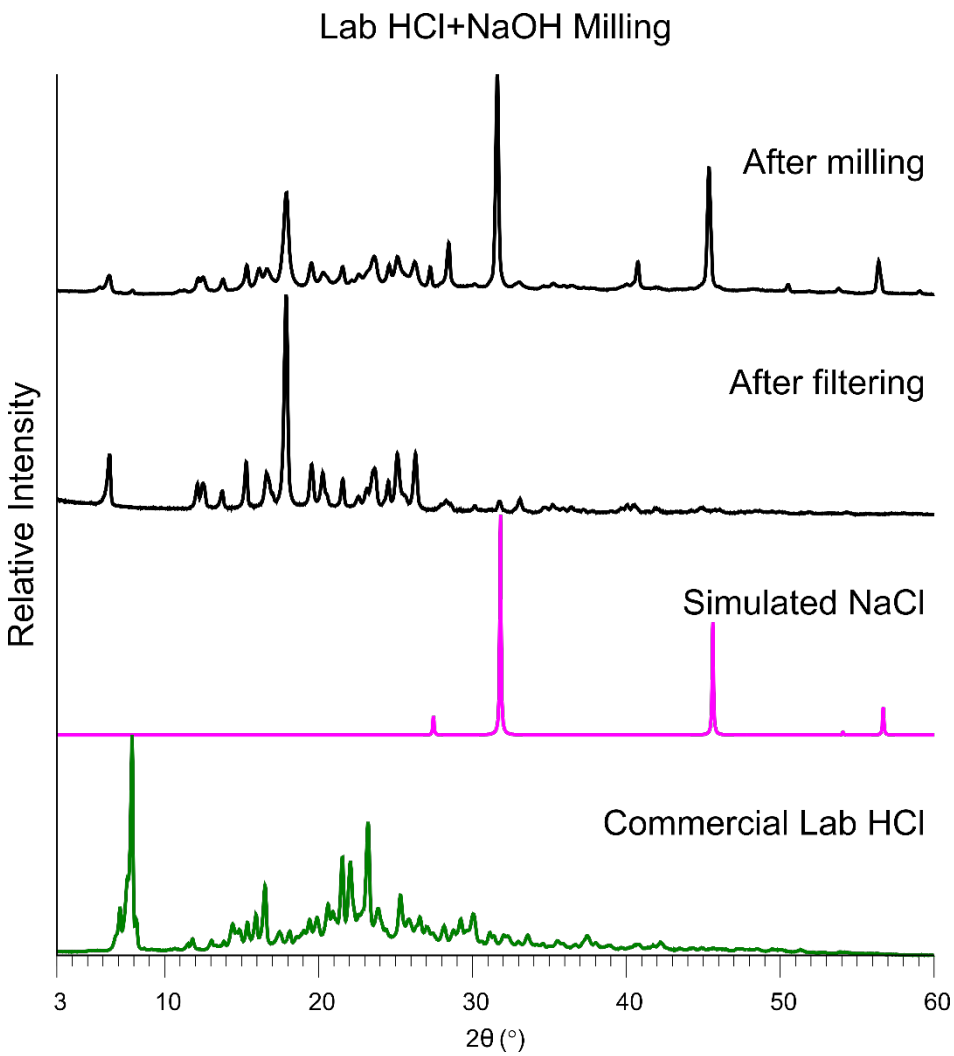

Figure S25. PXRD patterns of the commercial **Lab HCl** milling outcomes. Simulated pattern: NaCl 1000041 (COD).

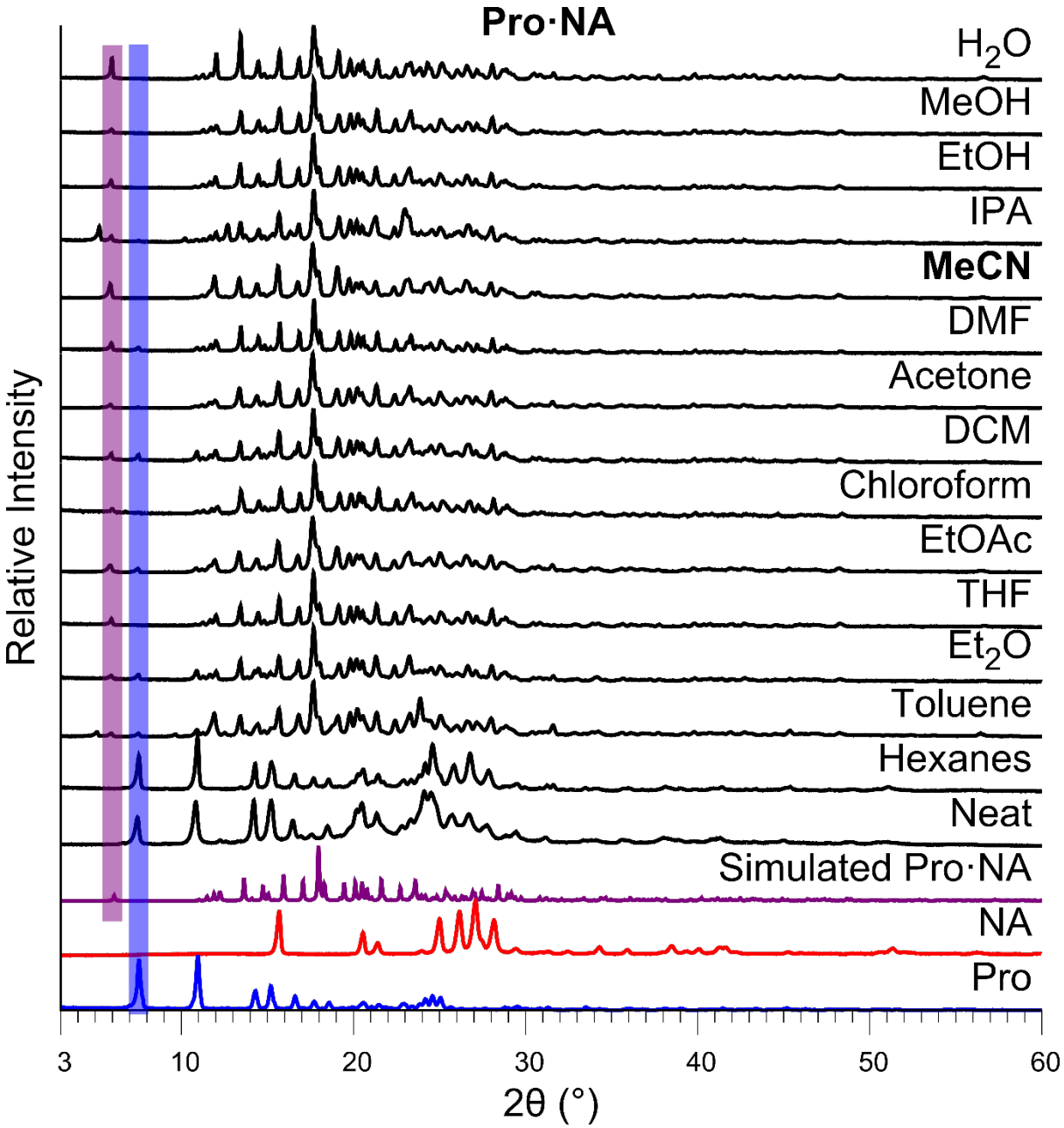

Figure S26. PXRD patterns illustrating the effect of solvent polarity on the outcome of the mechanochemical synthesis of **Pro·NA**. Solvents are ordered from the most polar (top) to the least with the solvent used to grow single crystals of the salt in bold. The purple (salt) and blue (free base beta blocker) highlighted peaks indicate the characteristic reference peaks used to determine each patterns' composition (pure salt, mixture of salt and components, components only, and presence of unknown phase(s)).

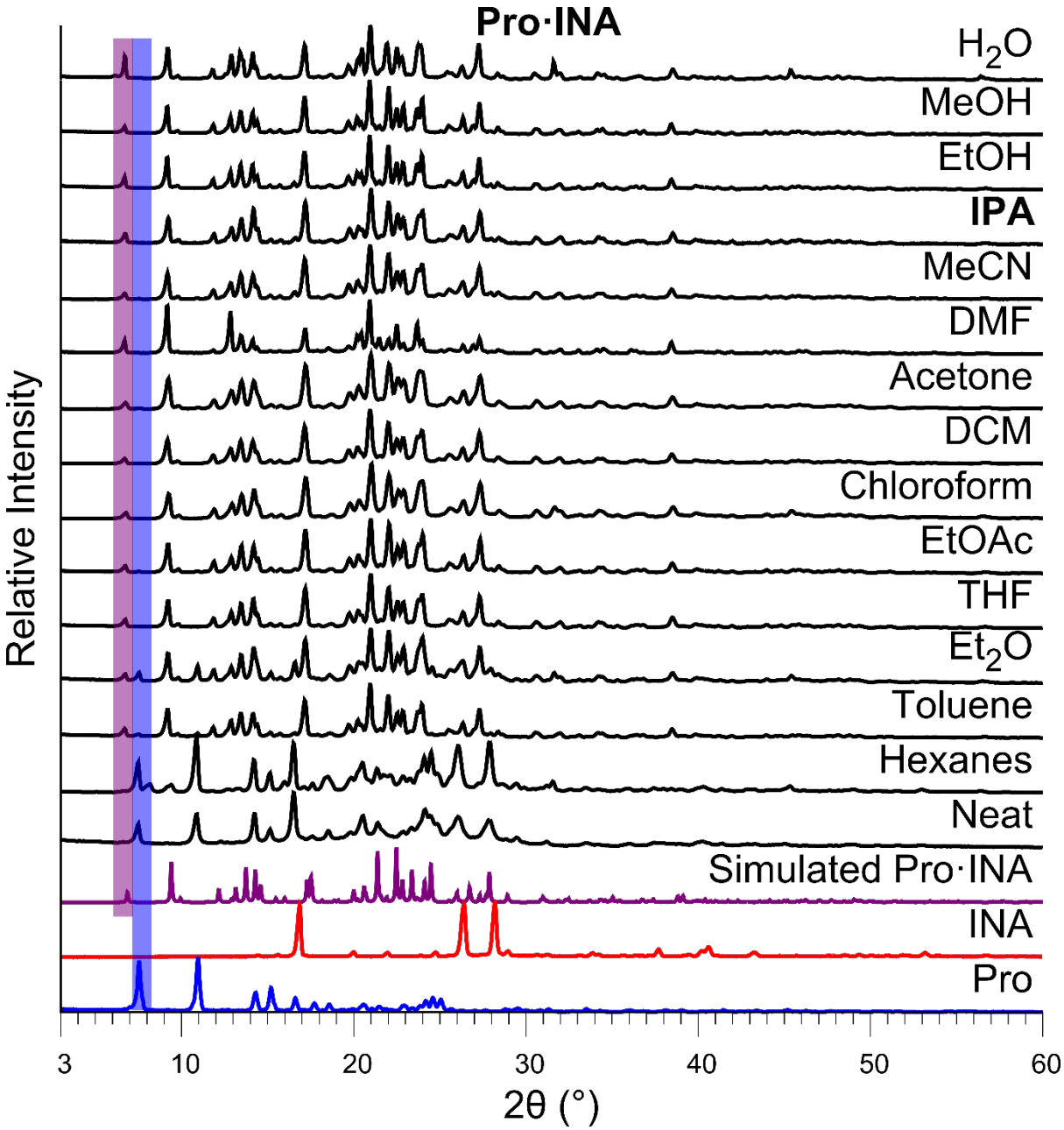

Figure S27. PXRD patterns illustrating the effect of solvent polarity on the outcome of the mechanochemical synthesis of **Pro·INA**. Solvents are ordered from the most polar (top) to the least with the solvent used to grow single crystals of the salt in bold. The purple (salt) and blue (free base beta blocker) highlighted peaks indicate the characteristic reference peaks used to determine each patterns' composition (pure salt, mixture of salt and components, components only, and presence of unknown phase(s)).

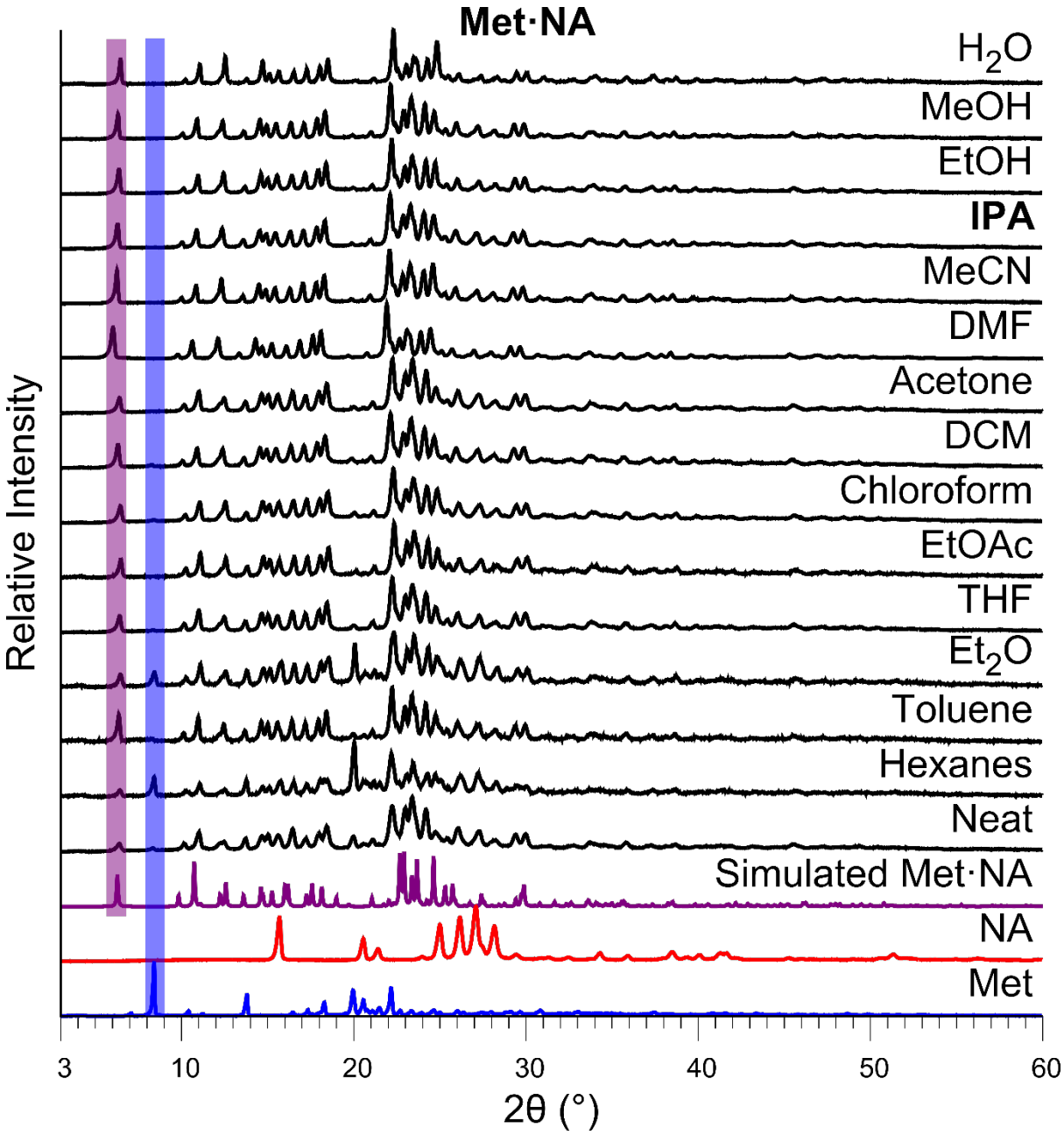

Figure S28. PXRD patterns illustrating the effect of solvent polarity on the outcome of the mechanochemical synthesis of **Met·NA**. Solvents are ordered from the most polar (top) to the least with the solvent used to grow single crystals of the salt in bold. The purple (salt) and blue (free base beta blocker) highlighted peaks indicate the characteristic reference peaks used to determine each patterns' composition (pure salt, mixture of salt and components, components only, and presence of unknown phase(s)).

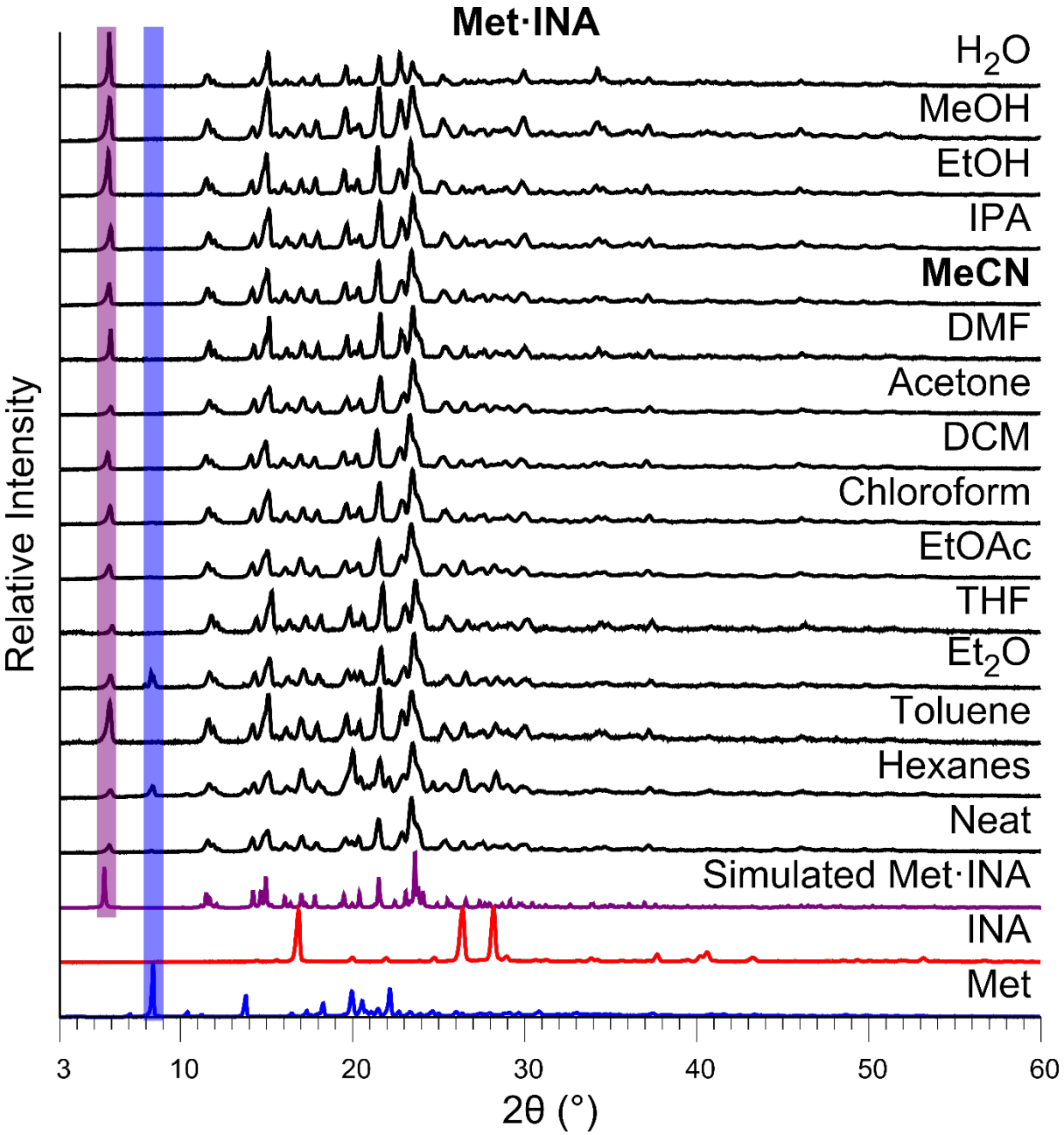

Figure S29. PXRD patterns illustrating the effect of solvent polarity on the outcome of the mechanochemical synthesis of **Met·INA**. Solvents are ordered from the most polar (top) to the least with the solvent used to grow single crystals of the salt in bold. The purple (salt) and blue (free base beta blocker) highlighted peaks indicate the characteristic reference peaks used to determine each patterns' composition (pure salt, mixture of salt and components, components only, and presence of unknown phase(s)).

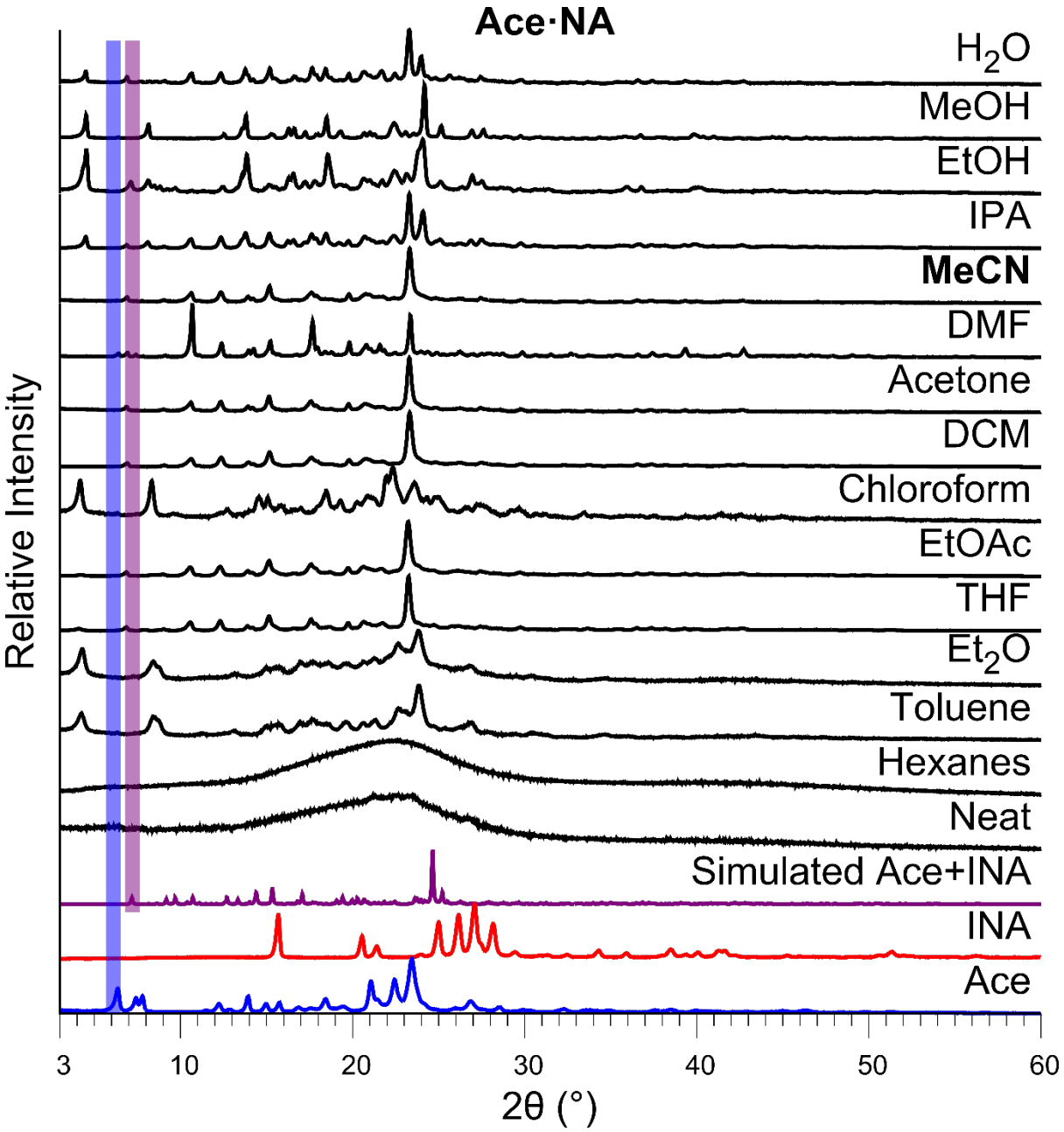

Figure S30. PXRD patterns illustrating the effect of solvent polarity on the outcome of the mechanochemical synthesis of **Ace·NA**. Solvents are ordered from the most polar (top) to the least with the solvent used to grow single crystals of the salt in bold. The purple (salt) and blue (free base beta blocker) highlighted peaks indicate the characteristic reference peaks used to determine each patterns' composition (pure salt, mixture of salt and components, components only, and presence of unknown phase(s)).

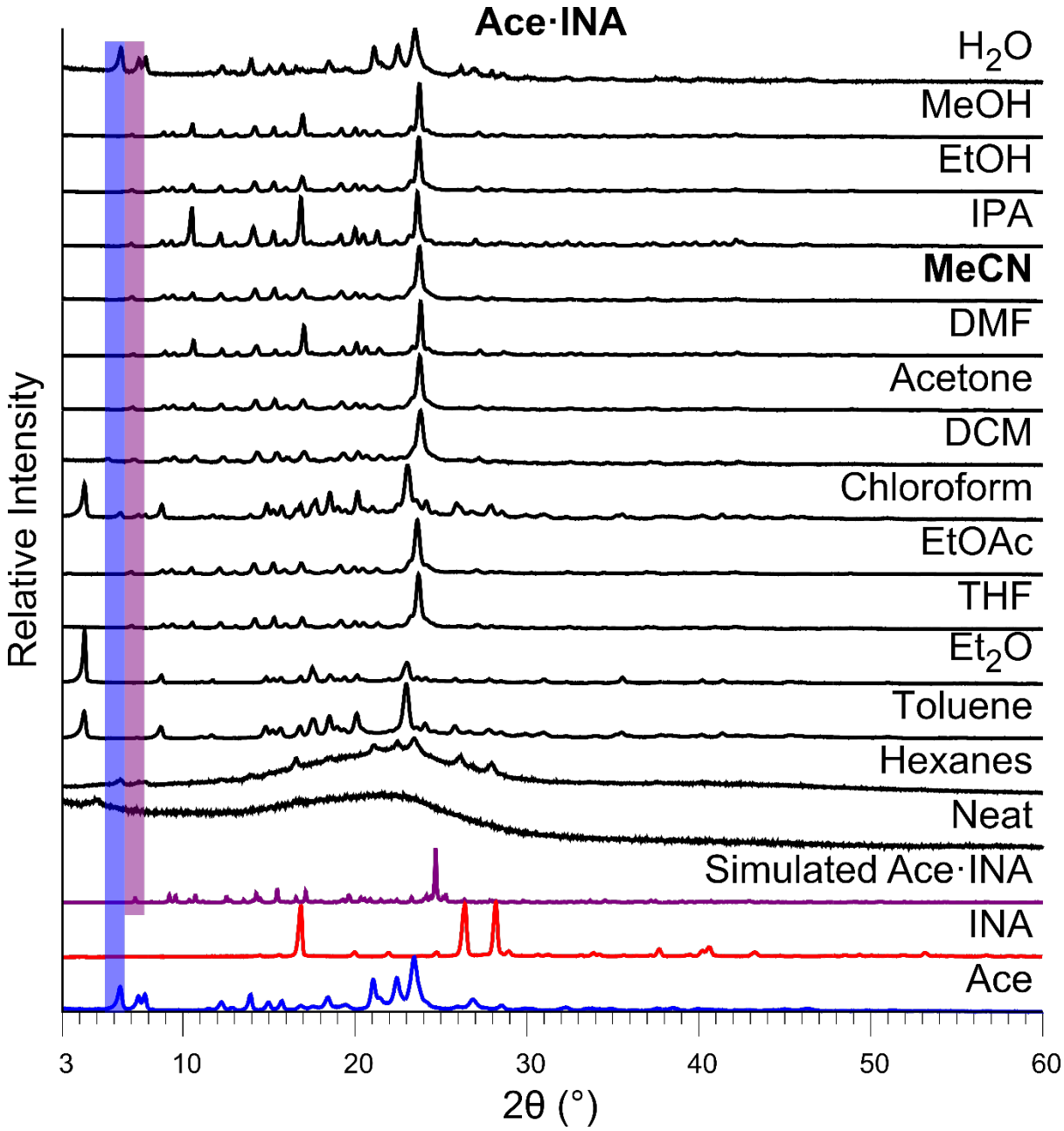

Figure S31. PXRD patterns illustrating the effect of solvent polarity on the outcome of the mechanochemical synthesis of **Ace·INA**. Solvents are ordered from the most polar (top) to the least with the solvent used to grow single crystals of the salt in bold. The purple (salt) and blue (free base beta blocker) highlighted peaks indicate the characteristic reference peaks used to determine each patterns' composition (pure salt, mixture of salt and components, components only, and presence of unknown phase(s)).

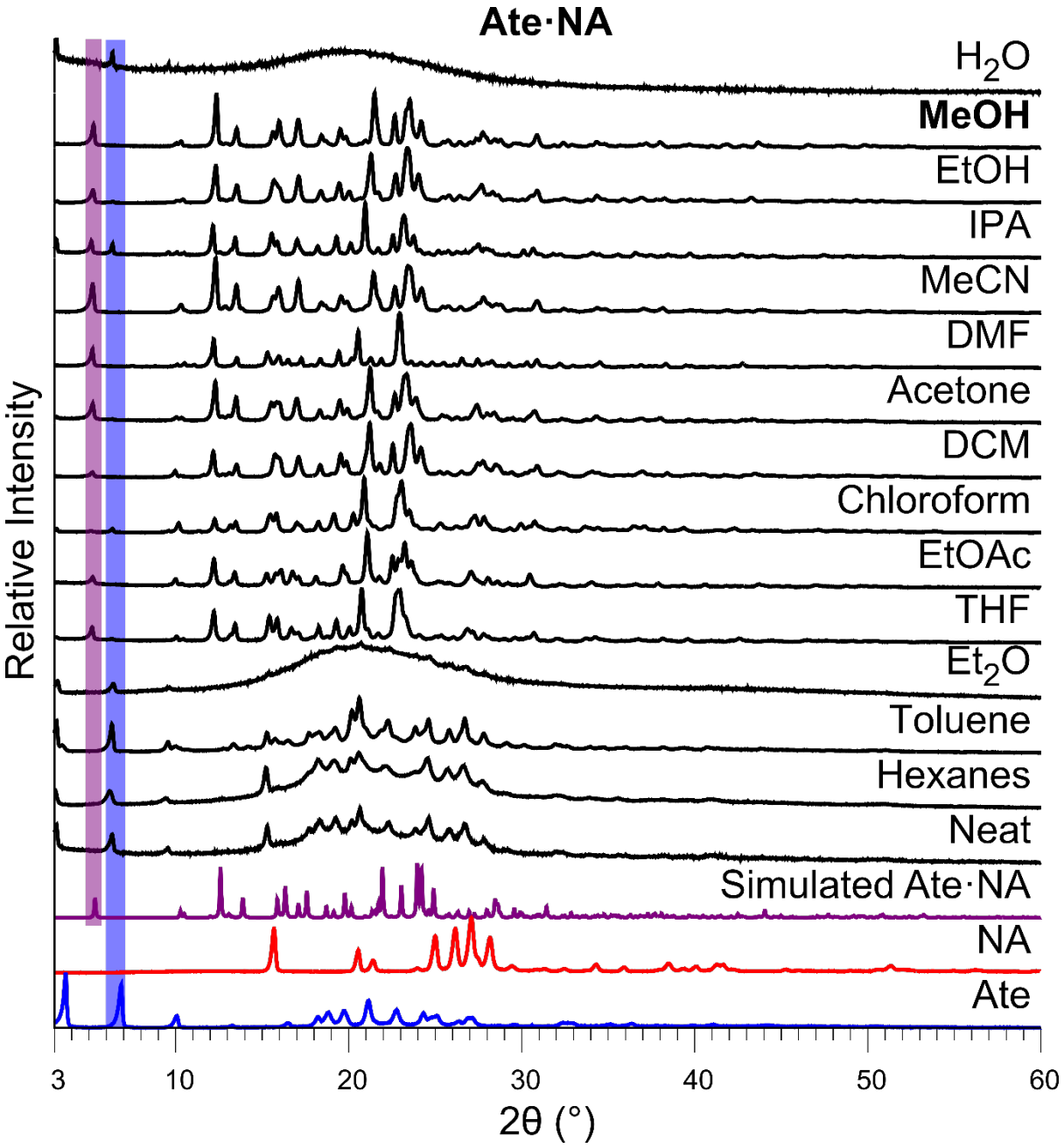

Figure S32. PXRD patterns illustrating the effect of solvent polarity on the outcome of the mechanochemical synthesis of **Ate·NA**. Solvents are ordered from the most polar (top) to the least with the solvent used to grow single crystals of the salt in bold. The purple (salt) and blue (free base beta blocker) highlighted peaks indicate the characteristic reference peaks used to determine each patterns' composition (pure salt, mixture of salt and components, components only, and presence of unknown phase(s)).

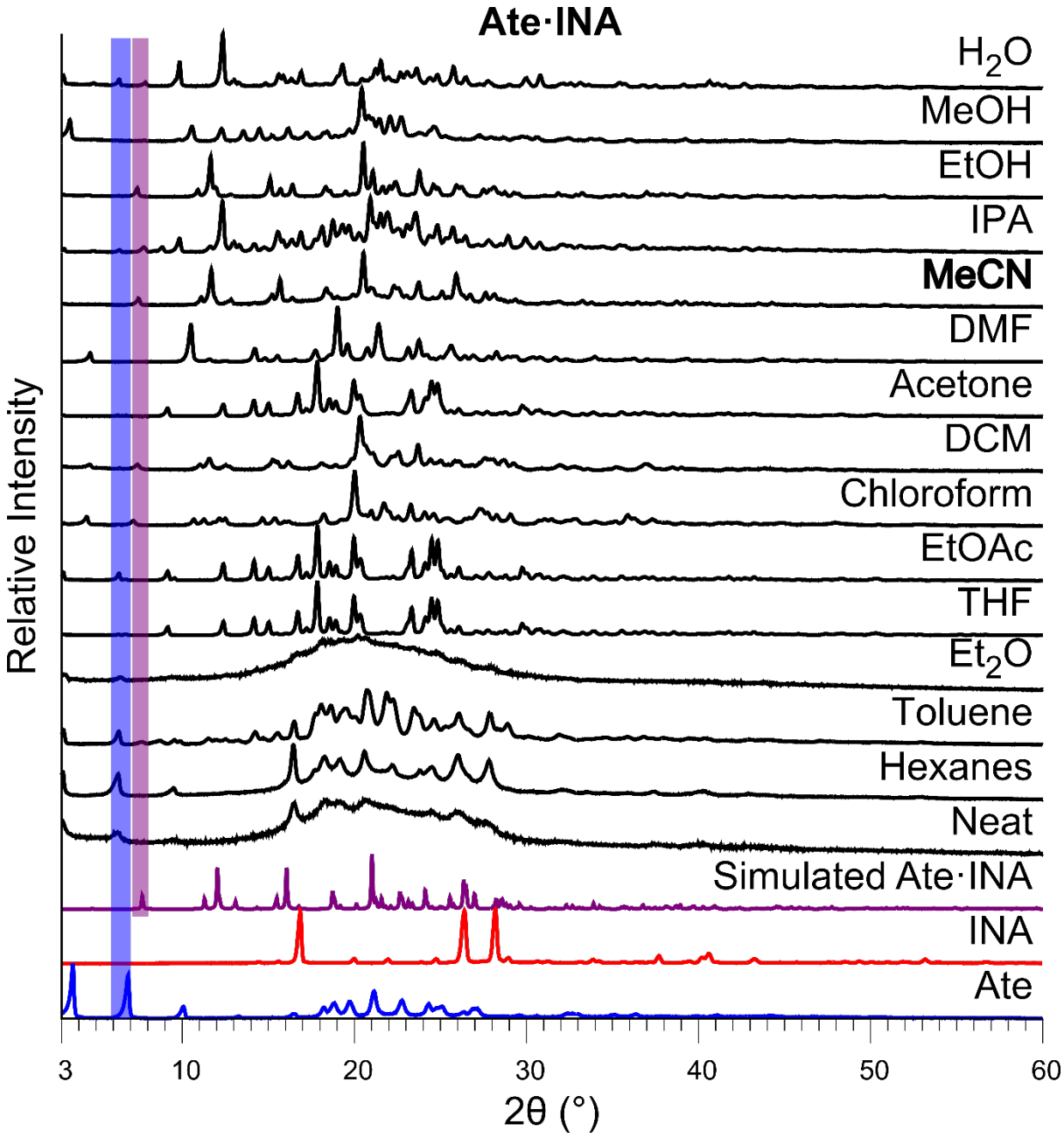

Figure S33. PXRD patterns illustrating the effect of solvent polarity on the outcome of the mechanochemical synthesis of **Ate·INA**. Solvents are ordered from the most polar (top) to the least with the solvent used to grow single crystals of the salt in bold. The purple (salt) and blue (free base beta blocker) highlighted peaks indicate the characteristic reference peaks used to determine each patterns' composition (pure salt, mixture of salt and components, components only, and presence of unknown phase(s)).

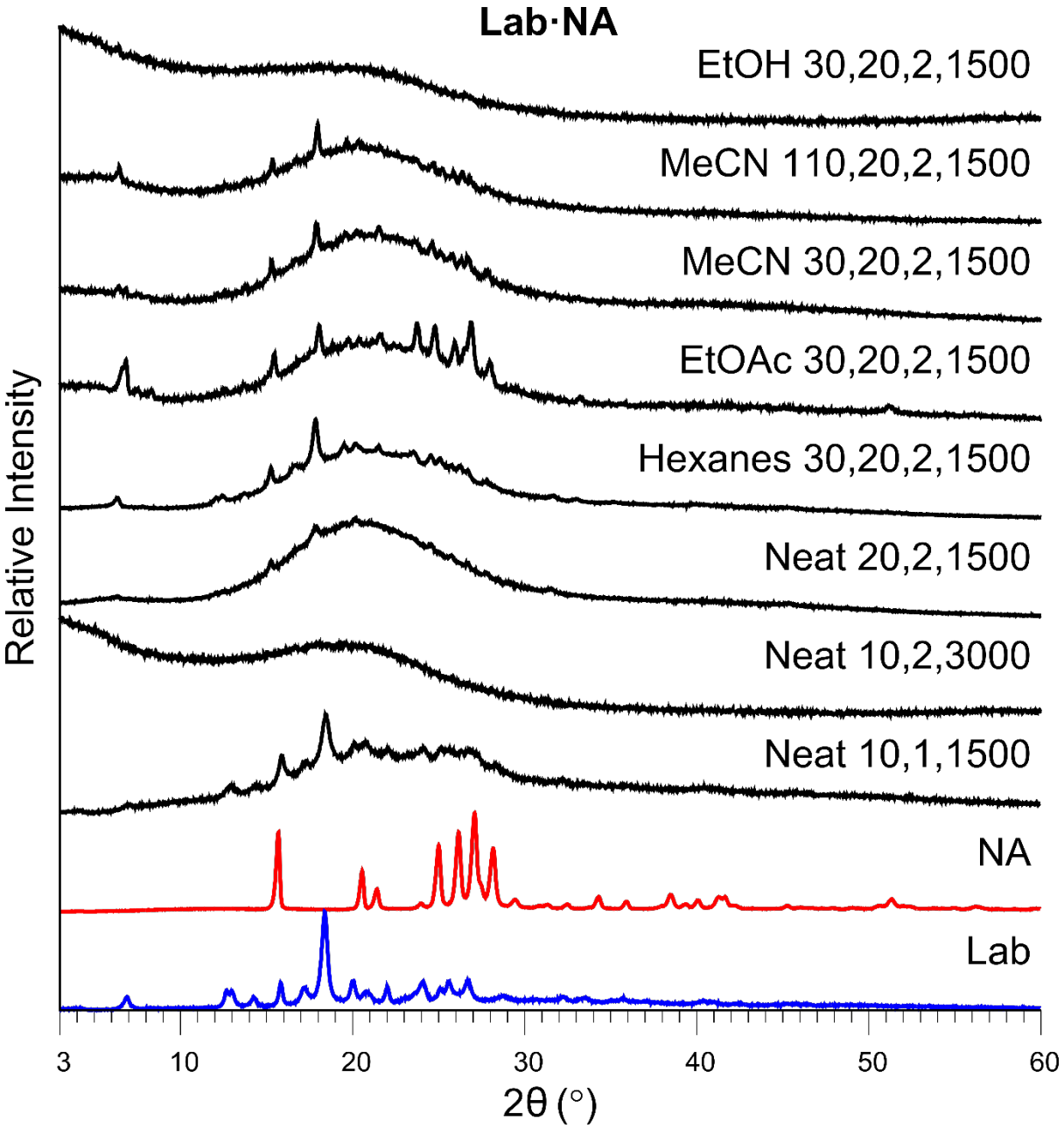

Figure S34. PXRD patterns illustrating a selection of conditions attempted towards the cocrystallization of **Lab·NA**. This was unsuccessful with only components and/or amorphous phases present. The numbers following the solvent label indicate mechanochemistry conditions of the solvent amount (μL), time (minutes), number of 7 mm ⌀ balls, and revolutions per minute (rpm). The neat milling conditions omit the solvent amount.

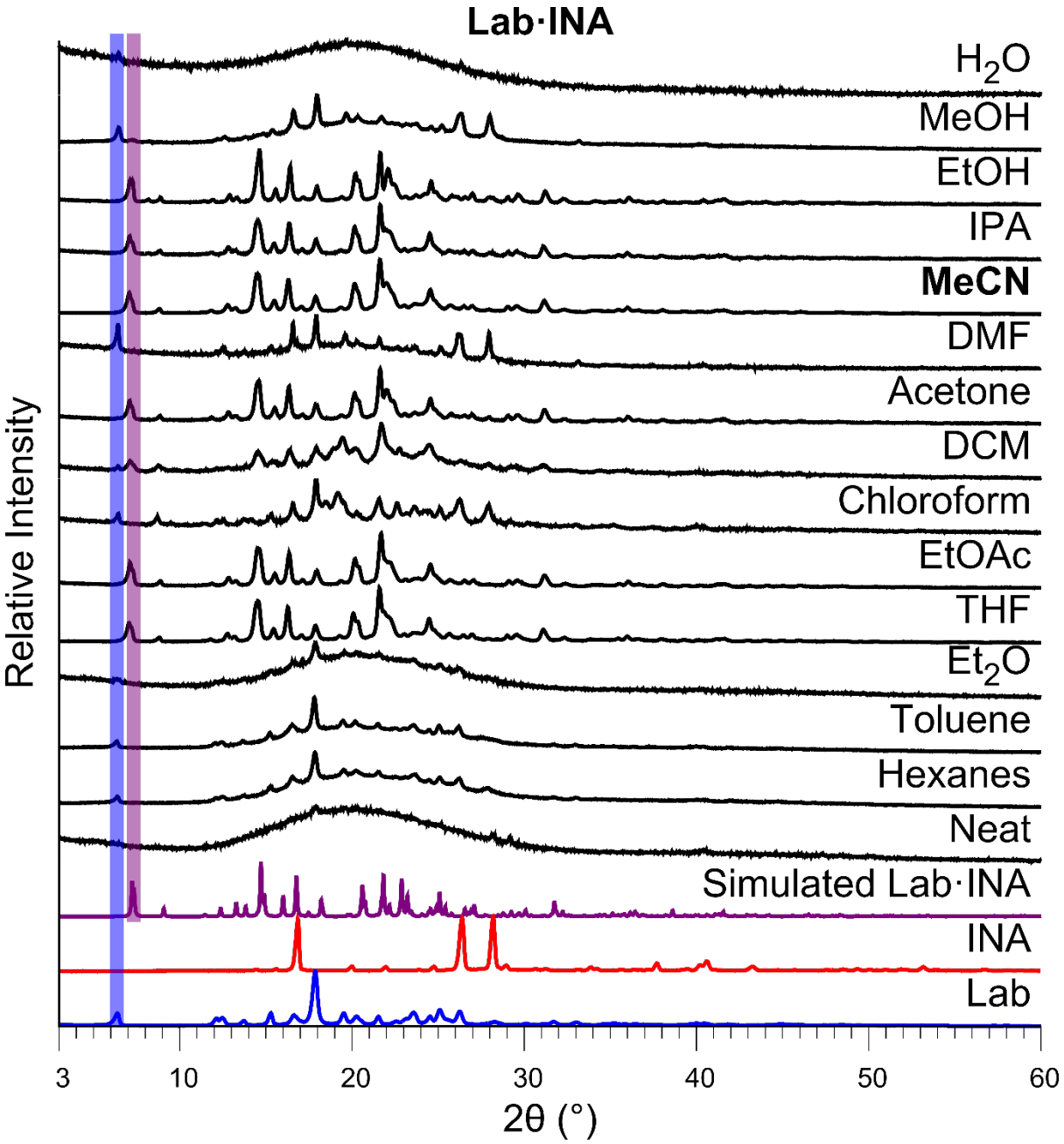

Figure S35. PXRD patterns illustrating the effect of solvent polarity on the outcome of the mechanochemical synthesis of **Lab·INA**. Solvents are ordered from the most polar (top) to the least with the solvent used to grow single crystals of the salt in bold. The purple (salt) and blue (free base beta blocker) highlighted peaks indicate the characteristic reference peaks used to determine each patterns' composition (pure salt, mixture of salt and components, components only, and presence of unknown phase(s)).

Table S7: Various parameters of the liquid additives used in LAG with the values of each parameter determining the liquid additive ordering in Table 3 (main text) and Tables S8-S10

Liquid additive	Polarity[a]	Hildebrand solubility parameter[b]	Dielectric constant[c]	Dipole moment[d]
H_2O	1.000	48.0	78.36	6.2
MeOH	0.762	29.7	32.66	5.9
EtOH	0.654	26.1	24.55	5.8
IPA	0.546	23.4	19.92	5.5
MeCN	0.460	24.8	35.94	13.0
DMF	0.386	24.7	36.71	12.7
Acetone	0.355	19.7	20.56	9.0
DCM	0.309	20.2	8.93	3.8
Chloroform	0.259	18.7	4.89	3.8
EtOAc	0.228	18.2	6.02	5.9
THF	0.207	18.5	7.58	5.8
Et_2O	0.117	15.4	4.20	3.8
Toluene	0.099	18.3	2.38	1.0
Hexanes	0.009	14.9	1.88	0.0

[a]Polarity values correspond to the empirical polarity parameter E_T^N as listed in Table A-1, Appendix A of *Solvents and Solvent Effects in Organic Chemistry*.[40]
[b]Hildebrand solubility parameter values taken from Table 18, Chapter 5 of the *CRC Handbook of Solubility Parameters and Other Cohesion Parameters*.[41]
[c]Dielectric constant values correspond to ε_r (relative permittivity) as listed in Table A-1, Appendix A of *Solvents and Solvent Effects in Organic Chemistry*.[40]
[d]Dipole moment values as listed in Table A-1, Appendix A of *Solvents and Solvent Effects in Organic Chemistry*.[40]

Table S8: Summary of the results of different liquid additives in the formation of the **beta blocker·NA/INA** salts with solvents ordered according to their Hildebrand solubility parameter (hexanes is lowest and H_2O is highest, see Table S7)[41]

Salt	Hexanes	Et_2O	EtOAc	Toluene	THF	Chloroform	Acetone	DCM	IPA	DMF	MeCN	EtOH	MeOH	H_2O
Pro·NA	x	~	~	~	√	√	~	~	~	~	√	√	√	√
Pro·INA	~	~	~	~	√	√	~	√	√	√	~	√	√	√
Met·NA	~	~	√	~	~	~	√	~	√	√	√	√	√	√
Met·INA	~	~	~	√	√	~	√	√	√	√	√	√	√	√
Ace·NA	x	*	~	*	~	*	√	√	~	~	√	*	*	~
Ace·INA	x	*	√	*	√	*	√	~	√	√	√	√	√	x
Ate·NA	x	x	√	x	~	~	~	√	~	~	√	~	√	x
Ate·INA	x	x	*	~	*	~	*	~	~	*	√	~	*	~
Lab·INA	x	x	√	x	√	*	√	~	√	x	√	√	~	x

	Key
√	Complete salt conversion. Thick box outline illustrates solvent from which single crystals were grown
~	Incomplete conversion where components and/or unknown phases(s) are present
x	No salt formation with only components present
*	Unknown phase(s) with or without components

Table S9: Summary of the results of different liquid additives in the formation of the **beta blocker·NA/INA** salts with solvents ordered according to their dielectric constant (hexanes is lowest and H_2O is highest, see Table S7)[40]

Salt	Hexanes	Toluene	Et_2O	Chloroform	EtOAc	THF	DCM	IPA	Acetone	EtOH	MeOH	MeCN	DMF	H_2O
Pro·NA	x	~	~	√	~	√	~	~	~	√	√	√	~	√
Pro·INA	~	~	~	√	~	√	√	√	~	√	√	~	√	√
Met·NA	~	~	~	~	√	~	~	√	√	√	√	√	√	√
Met·INA	~	√	~	~	~	√	√	√	√	√	√	√	√	√
Ace·NA	x	*	*	*	~	~	√	~	√	*	*	√	~	~
Ace·INA	x	*	*	*	√	√	~	√	√	√	√	√	√	x
Ate·NA	x	x	x	~	√	~	√	~	~	~	√	√	~	x
Ate·INA	x	~	x	~	*	*	~	~	*	~	*	√	*	~
Lab·INA	x	x	x	*	√	√	~	√	√	√	~	√	x	x

Key

√	Complete salt conversion. Thick box outline illustrates solvent from which single crystals were grown
~	Incomplete conversion where components and/or unknown phases(s) are present
x	No salt formation with only components present
*	Unknown phase(s) with or without components

Table S10: Summary of the results of different liquid additives in the formation of the **beta blocker·NA/INA** salts with solvents ordered according to their dipole moment (hexanes is lowest and MeCN is highest, see Table S7)[40]

Salt	Hexanes	Toluene	Et_2O	Chloroform	DCM	IPA	THF	EtOH	EtOAc	MeOH	H_2O	Acetone	DMF	MeCN
Pro·NA	x	~	~	√	~	~	√	√	~	√	√	~	~	√
Pro·INA	~	~	~	√	√	√	√	√	~	√	√	~	√	~
Met·NA	~	~	~	~	~	√	~	√	√	√	√	√	√	√
Met·INA	~	√	~	~	√	√	√	√	~	√	√	√	√	√
Ace·NA	x	*	*	*	√	~	~	*	~	*	~	√	~	√
Ace·INA	x	*	*	*	~	√	√	√	√	√	x	√	√	√
Ate·NA	x	x	x	~	√	~	~	~	√	√	x	~	~	√
Ate·INA	x	~	x	~	~	~	*	~	*	*	~	*	*	√
Lab·INA	x	x	x	*	~	√	√	√	√	~	x	√	x	√

Key

√	Complete salt conversion. Thick box outline illustrates solvent from which single crystals were grown
~	Incomplete conversion where components and/or unknown phases(s) are present
x	No salt formation with only components present
*	Unknown phase(s) with or without components

6. Nuclear magnetic resonance (NMR) spectroscopy

^{1}H NMR spectra of the phase pure powders of the **beta blocker·NA/INA** salts were obtained in DMSO-d_6 on a Bruker Avance III 500 MHz Spectrometer. Chemical shifts are reported as δ (ppm) with shifts referenced to residual nondeuterated DMSO (2.50 ppm). Coupling patterns were abbreviated as follows: s-singlet, d-doublet, dd-doublet of doublets, t-triplet, m-multiplet. In all cases, labile alcohol and amine protons were not observed due to exchange with water in the deuterated DMSO. Amide protons (in the case of **Ace**, **Ate** and **Lab**) were observed and were identified using a D_2O shake.

Pro·NA

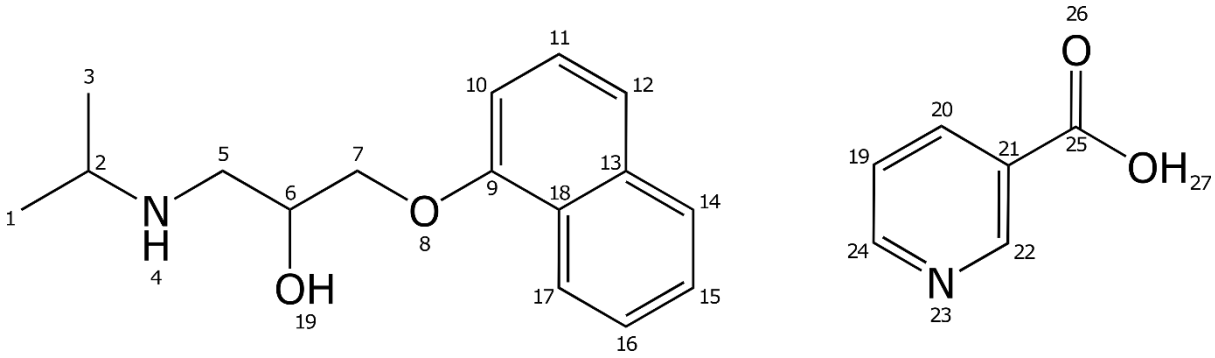

^{1}H NMR (500 MHz, DMSO) δ: 9.06-9.05 (m, 1H, H-22), 8.60-8.59 (m, 1H, H-24), 8.29-8.27 (m, 1H, H-17), 8.21-8.19 (m, 1H, H-14), 7.87-7.85 (d, 1H, H-20), 7.54-7.46 (m, 3H, H-12, H-15, H-16), 7.41-7.38 (m, 2H, H-11, H-19), 6.97-6.96 (d, 1H, H-10), 4.42-4.38 (m, 1H, H-6), 4.20-4.14 (m, 2H, H-7), 3.38-3.33 (m, 1H, H-2), 3.28-3.25 (m, 1H, H-5), 3.14-3.09 (m, 1H, H-5), 1.32-1.26 (dd, 6H, H-1, H-3).

Pro·INA

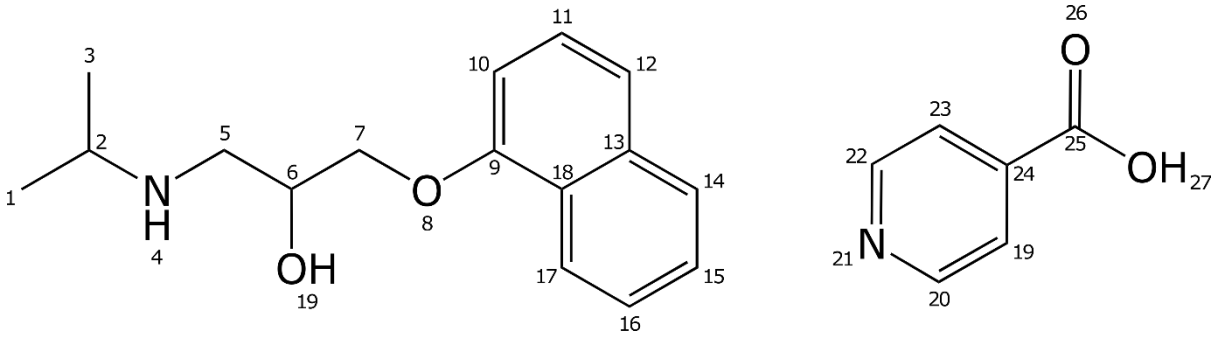

^{1}H NMR (500 MHz, DMSO) δ: 8.61-8.59 (m, 2H, H-20, H-22), 8.29-8.27 (d, 1H, H-17), 7.87-7.85 (d, 1H, H-14), 7.78-7.75 (m, 2H, H-19, H-23), 7.53-7.45 (m, 3H, H-12, H-15, H-16), 7.41-7.38 (m, 1H, H-11), 6.97-6.95 (d, 1H, H-10), 4.45-4.38 (m, 1H, H-6), 4.21-4.14 (m, 2H, H-7), 3.41-3.36 (m, 1H, H-2), 3.31-3.27 (m, 1H, H-5), 3.17-3.12 (m, 1H, H-5), 1.31-1.27 (m, 6H, H-1, H-3).

Met·NA

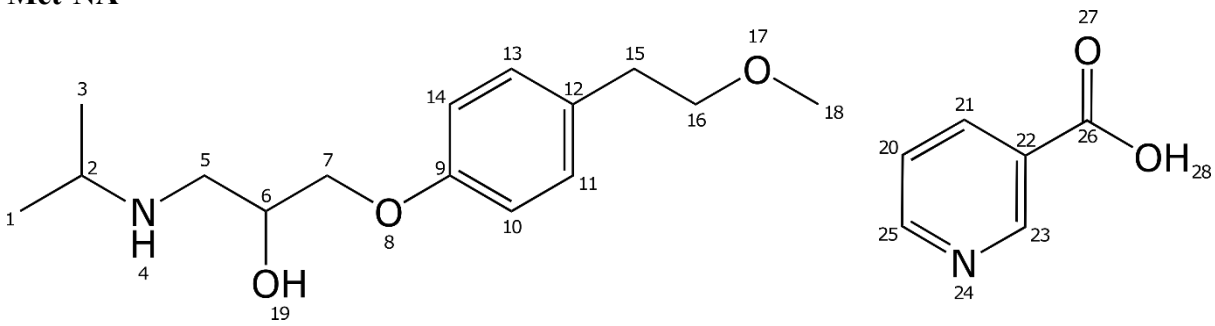

^{1}H NMR (500 MHz, DMSO) δ: 9.02 (m, 1H, H-23), 8.59-8.58 (m, 1H, H-25), 8.19-8.16 (m, 1H, H-21), 7.39-7.37 (m, 1H, H-20), 7.13-7.11 (m, 2H, H-11, H-13), 6.87-6.84 (m, 2H, H-10, H-14), 4.24-4.21 (m, 1H, H-6), 3.98-3.92 (m, 2H, H-7), 3.47-3.45 (t, 2H, H-16), 3.32-3.27 (m, 1H, H-2), 3.22 (s, 3H, H-18), 3.14-3.10 (m, 1H, H-5), 2.98-2.93 (m, 1H, H-5), 2.73-2.70 (t, 2H, H-15), 1.27-1.23 (m, 6H, H-1, H-3).

Met·INA

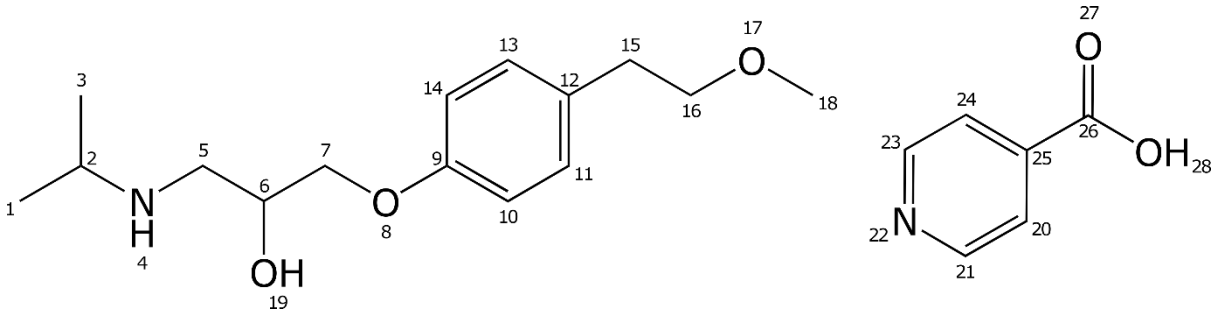

^{1}H NMR (500 MHz, DMSO) δ: 8.60-8.59 (m, 2H, H-21, H-23), 7.73-7.72 (m, 2H, H-20, H-24), 7.14-7.11 (d, 2H, H-11, H-13), 6.87-6.85 (d, 2H, H-10, H-14), 4.25-4.20 (m, 1H, H-6), 3.98-3.92 (m, 2H, H-7), 3.47-3.45 (t, 2H, H-16), 3.35-3.31 (m, 1H, H-2), 3.22 (s, 3H, H-18), 3.15-3.11 (m, 1H, H-5), 2.99-2.95 (m, 1H, H-5), 2.73-2.70 (t, 2H, H-15), 1.27-1.24 (m, 6H, H-1, H-3).

Ace·NA

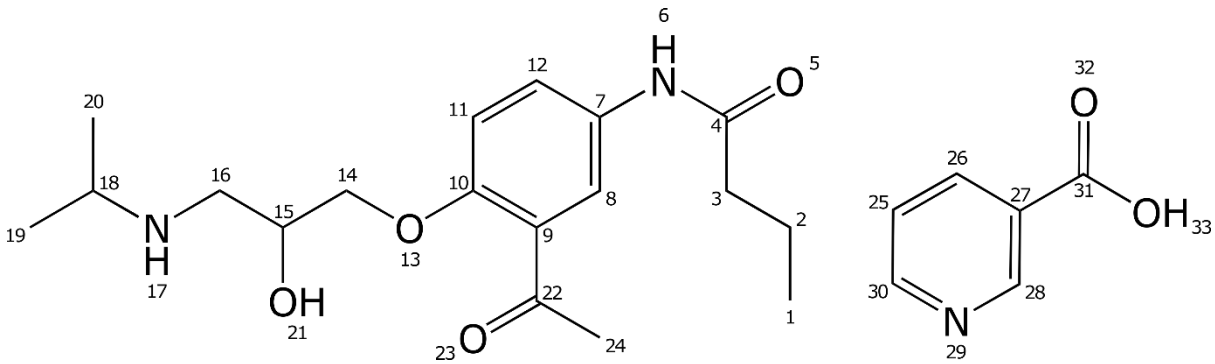

^{1}H NMR (500 MHz, DMSO) δ: 9.94 (s, 1H, H-6), 9.01 (s, 1H, H-28), 8.57-8.56 (m, 1H, H-30), 8.17-8.14 (m, 1H, H-26), 7.82 (m, 1H, H-8) 7.78-7.76 (m, 1H, H-12), 7.37-7.35 (m, 1H, H-25), 7.12-7.10 (d, 1H, H-11), 4.27-4.26 (m, 1H, H-15), 4.11-4.08 (m, 2H, H-14), 3.29-3.23 (m, 1H, H-18), 3.14-3.12 (m, 1H, H-16), 3.00-2.95 (m, 1H, H-16), 2.57 (s, 3H, H-24), 2.26-

2.23 (t, 2H, H-3), 1.63-1.55 (m, 2H, H-2), 1.24-1.22 (m, 6H, H-19, H-20), 0.91-0.88 (t, 3H, H-1).

Ace·INA

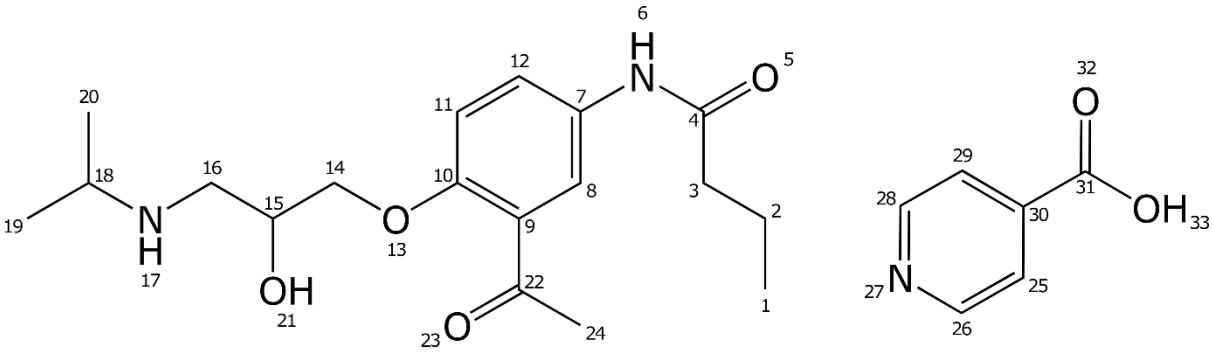

^{1}H NMR (500 MHz, DMSO) δ: 9.95 (s, 1H, H-6), 8.58-8.57 (m, 2H, H-26, H-28), 7.82 (m, 1H, H-8), 7.78-7.76 (m, 1H, H-12), 7.72-7.70 (m, 2H, H-25, H-29), 7.12-7.10 (d, 1H, H-11), 4.30-4.26 (m, 1H, H-15), 4.10-4.09 (m, 2H, H-14), 3.33-3.28 (m, 1H, H-18), 3.18-3.14 (m, 1H, H-16), 3.02-2.98 (m, 1H, H-16), 2.57 (s, 3H, H-24), 2.26-2.23 (t, 2H, H-3), 1.63-1.55 (m, 2H, H-2), 1.26-1.23 (dd, 6H, H-19, H-20), 0.91-0.88 (t, 3H, H-1).

Ate·NA

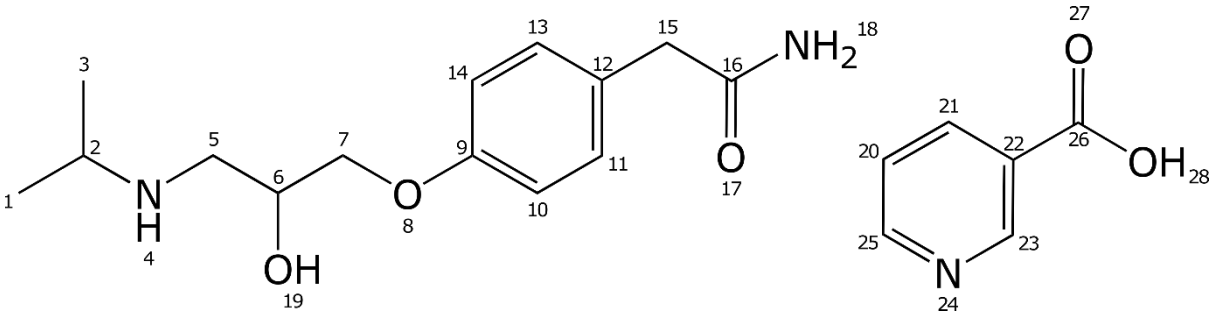

^{1}H NMR (500 MHz, DMSO) δ: 9.02-9.01 (m, 1H, H-23), 8.58-8.57 (m, 1H, H-25), 8.18-8.16 (m, 1H, H-21), 7.44 (s, 1H, H-18), 7.38-7.36 (m, 1H, H-20), 7.17-7.15 (m, 2H, H-11, H-13), 6.89-6.86 (m, 2H, H-10, H-14), 6.85 (s, 1H, H-18), 4.23-4.19 (m, 1H, H-6), 3.98-3.92 (m, 2H, H-7), 3.31-3.25 (m, 3H, H-2, H-15), 3.17 (s, MeOH solvate), 3.12-3.08 (m, 1H, H-5), 2.97-2.92 (m, 1H, H-5), 1.25-1.22 (m, 6H, H-1, H-3).

Ate·INA

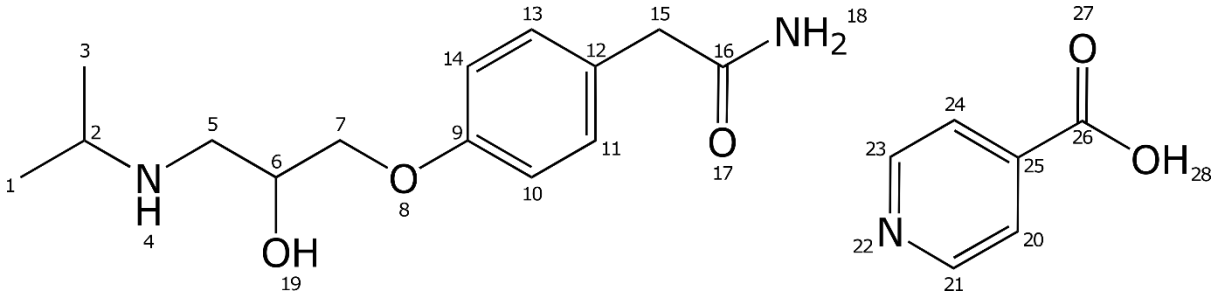

^{1}H NMR (500 MHz, DMSO) δ: 8.58-8.57 (m, 2H, H-21, H-23), 7.72-7.71 (m, 2H, H-20, H-24), 7.44 (s, 1H, H-18), 7.18-7.15 (m, 2H, H-11, H-13), 6.89-6.86 (m, 2H, H-10, H-14), 6.85 (s, 1H, H-18), 4.21-4.17 (m, 1H, H-6), 3.98-3.92 (m, 2H, H-7), 3.29 (s, 2H, H-15), 3.27-3.24 (m, 1H, H-2), 3.11-3.08 (m, 1H, H-5), 2.96-2.91 (m, 1H, H-5), 2.08 (s, MeCN solvate), 1.25-1.22 (dd, 6H, H-1, H-3).

Lab·INA

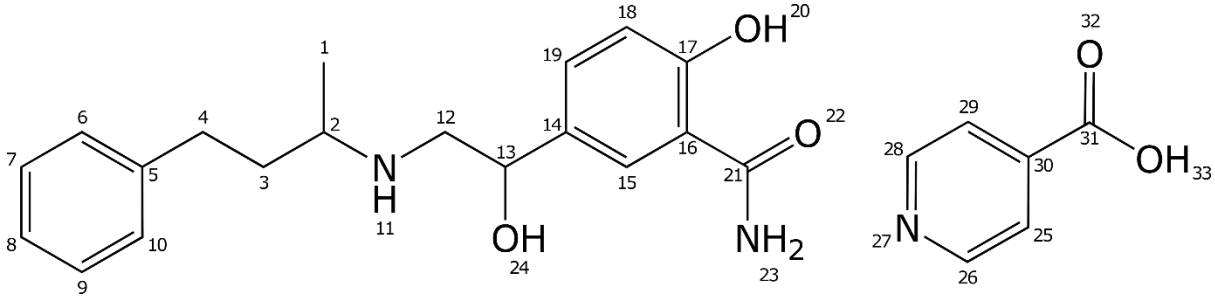

^{1}H NMR (500 MHz, DMSO) δ: 8.61-8.59 (m, 2H, H-26, H-28), 8.51 (s, 1H, H-23), 7.93-7.92 (m, 1H, H-15/H-19), 7.90 (s, 1H, H-23), 7.76-7.74 (m, 2H, H-25, H-29), 7.47-7.44 (m, 1H, H-19/H-15), 7.28-7.25 (m, 2H, aromatic ring protons H-6 to H-10), 7.23-7.16 (m, 3H, aromatic ring protons H-6 to H-10), 6.92-6.90 (m, 1H, H-18), 4.92-4.87 (m, 1H, H-13), 3.18-3.09 (m, 2H, H-2, H-12), 3.03-2.97 (m, 1H, H-12), 2.74-2.68 (m, 1H, H-4), 2.62-2.54 (m, 1H, H-4), 2.14-2.08 (m, 1H, H-3), 1.83-1.72 (m, 1H, H-3), 1.31-1.28 (m, 3H, H-1).

Figure S36. Pro·NA ^{1}H NMR spectrum

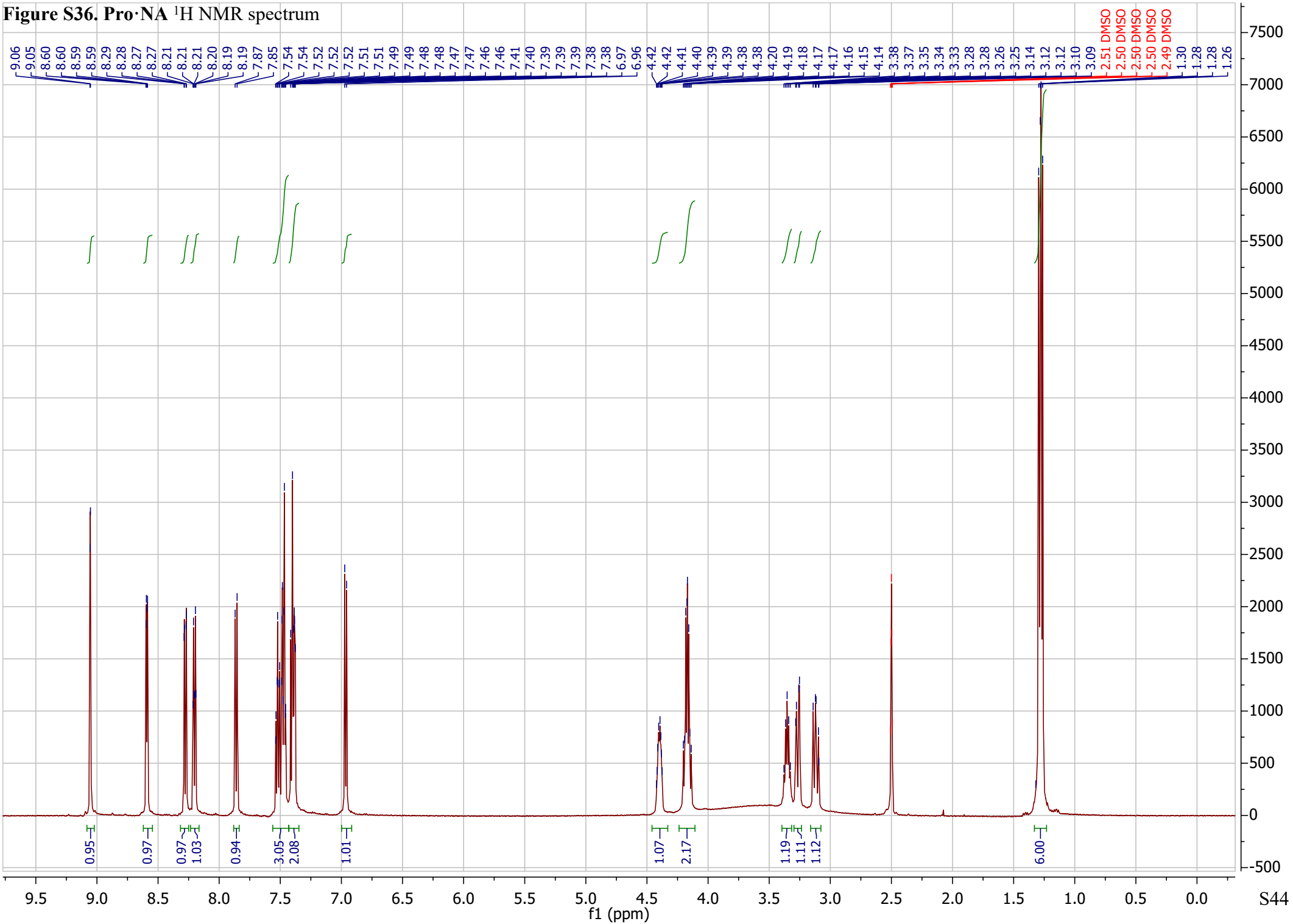

Figure S37. Pro·INA ^{1}H NMR spectrum

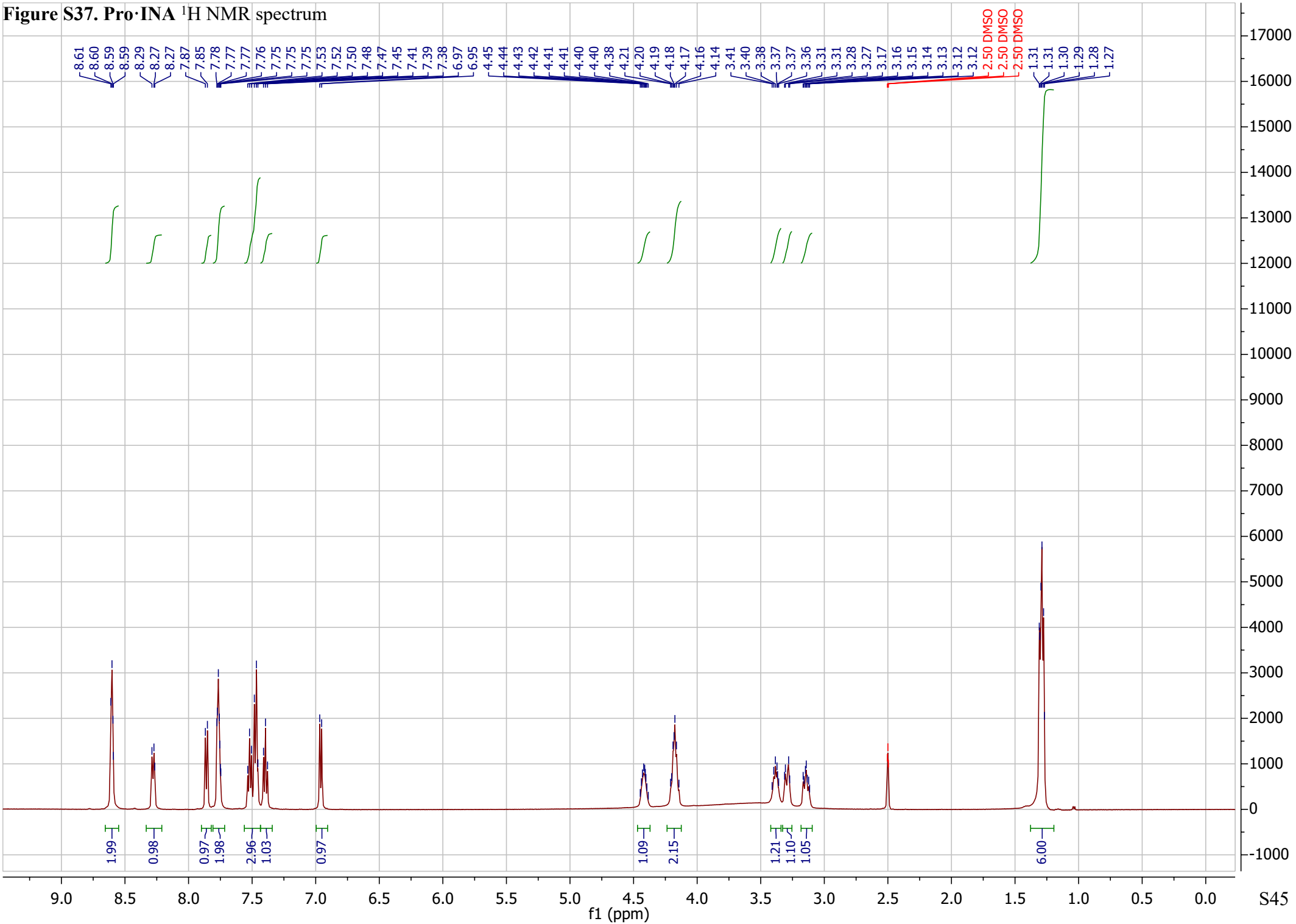

Figure S38. Met·NA ^{1}H NMR spectrum

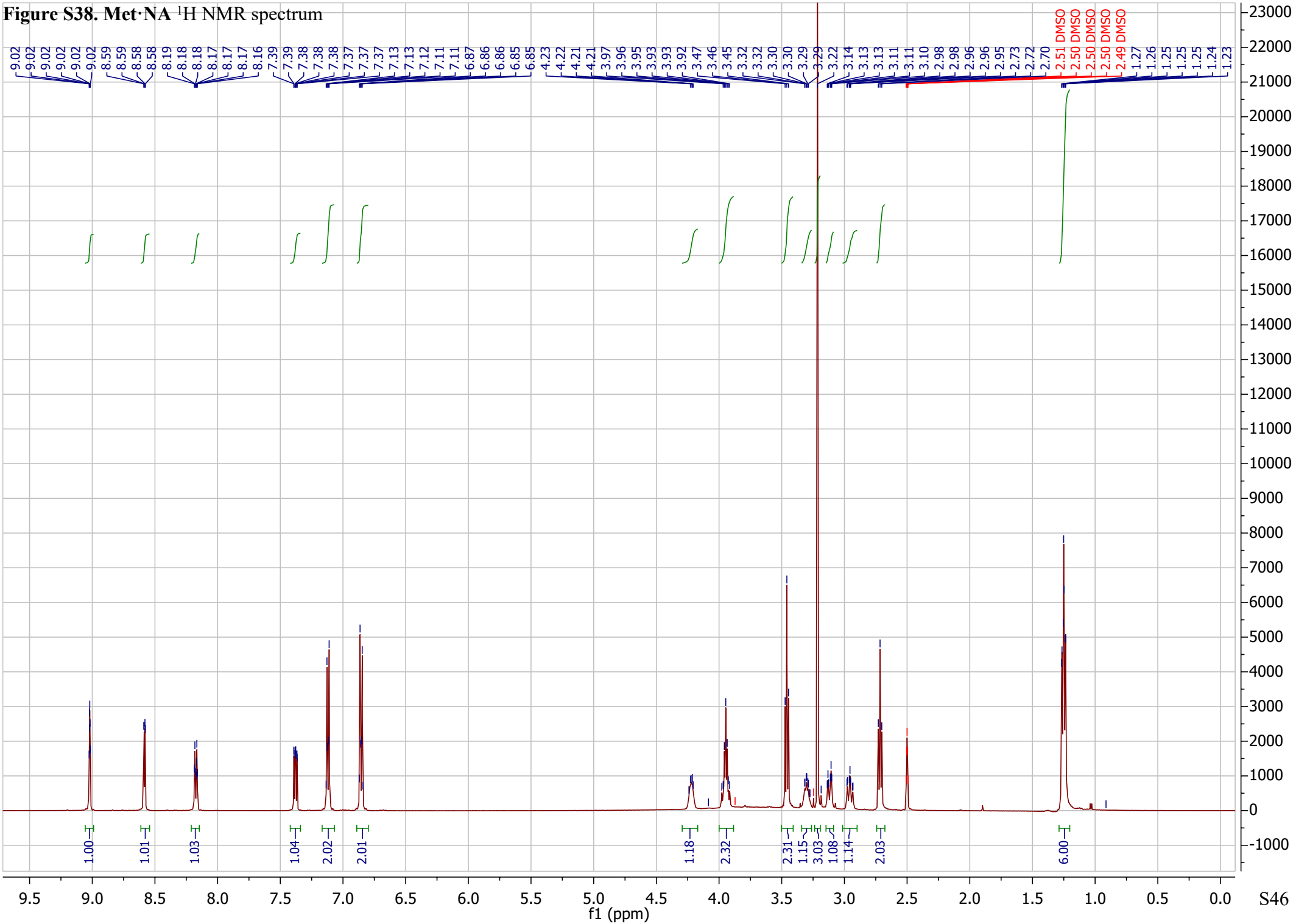

Figure S39. Met·INA ^{1}H NMR spectrum

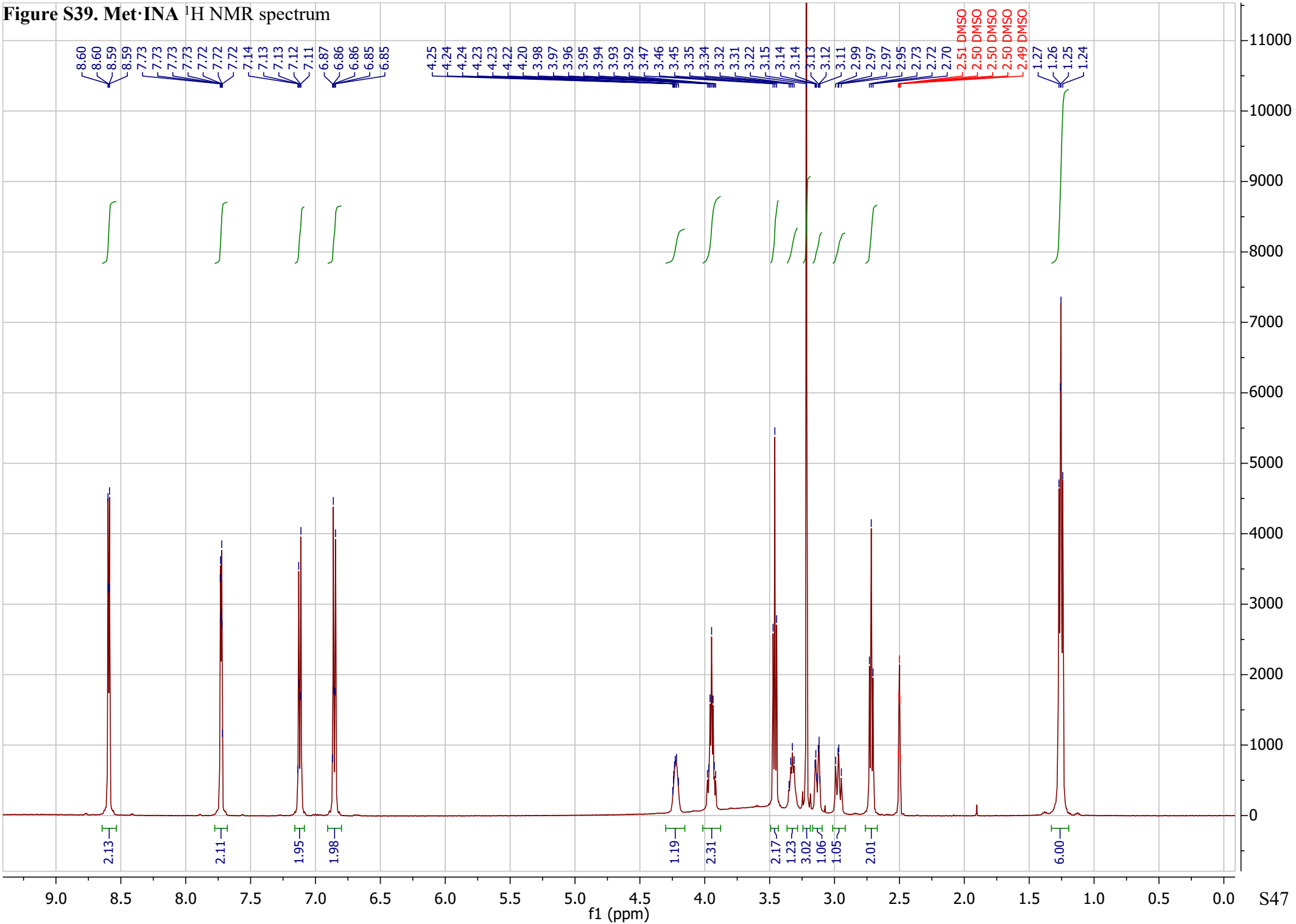

Figure S40. Ace·NA ^{1}H NMR spectrum

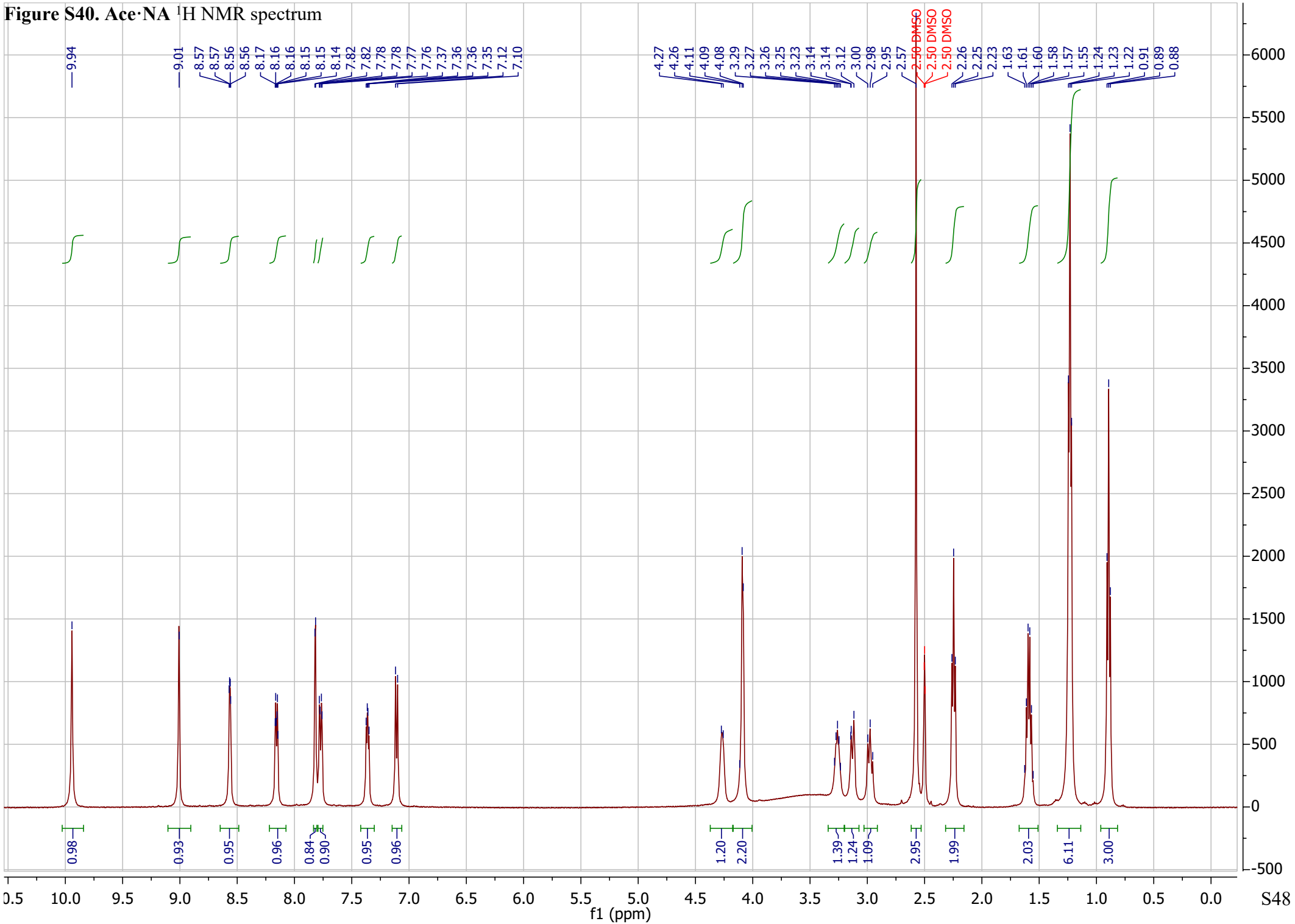

Figure S41. Ace·INA ^{1}H NMR spectrum

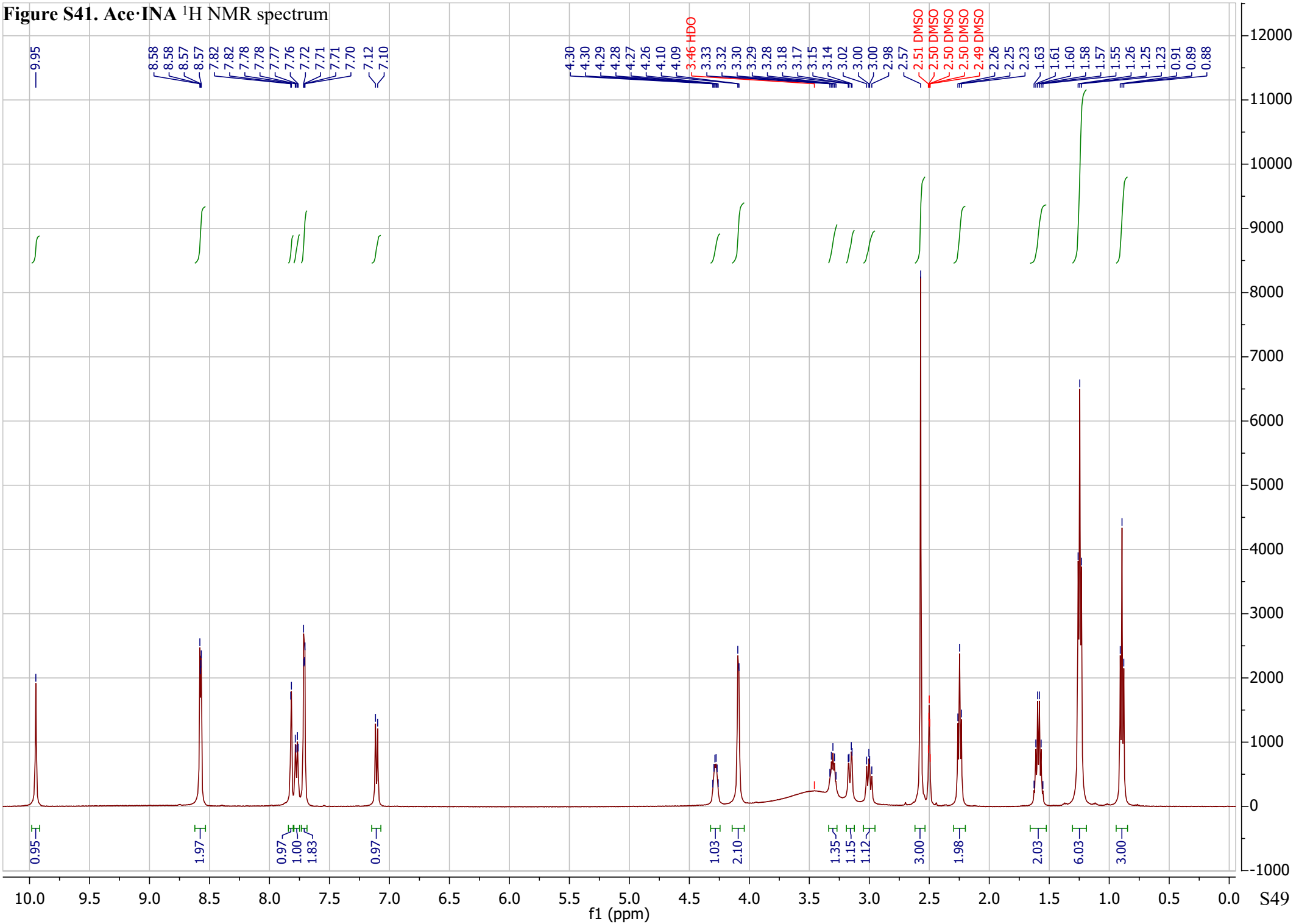

Figure S42. Ate·NA ^{1}H NMR spectrum

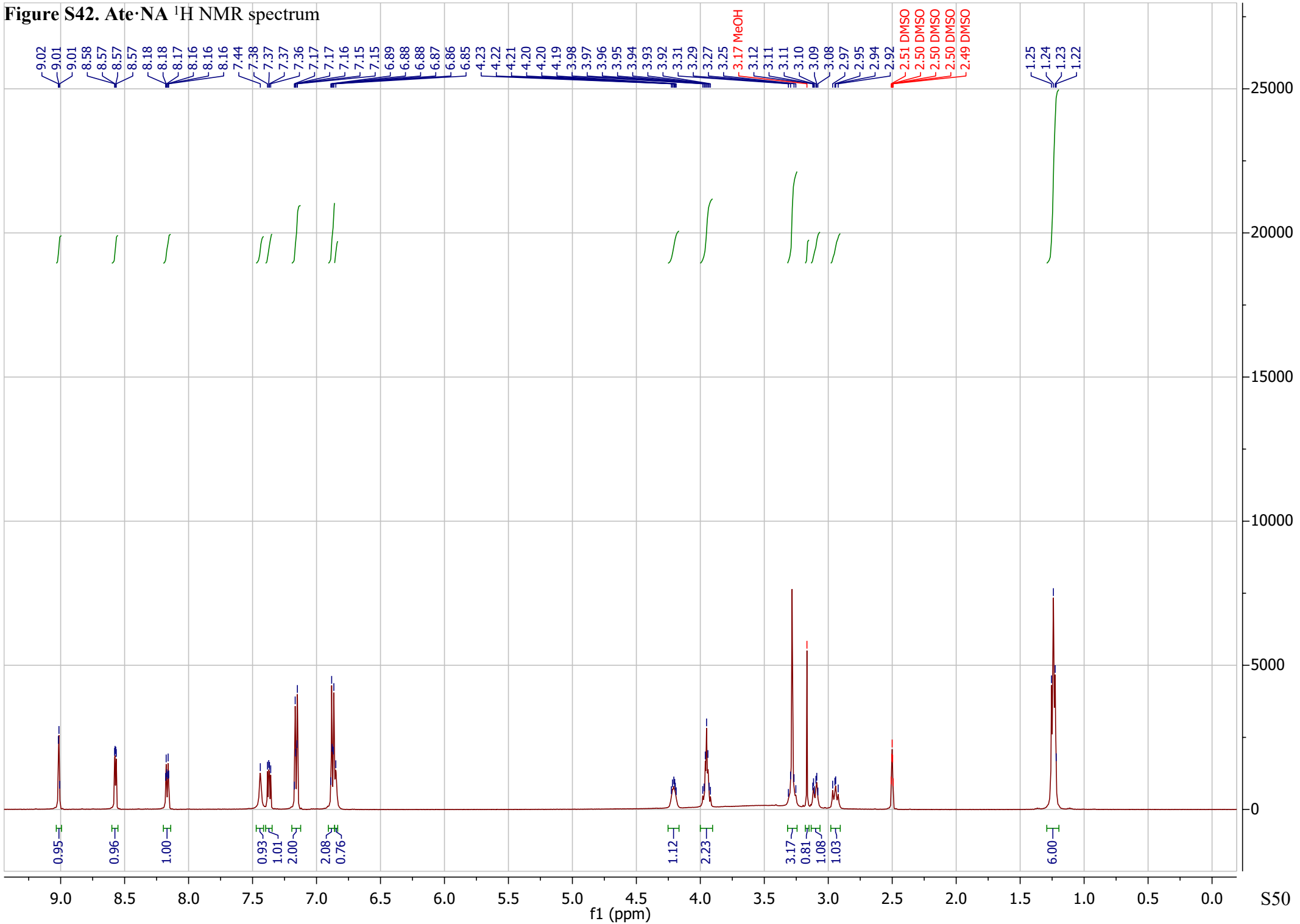

Figure S43. Ate·INA ^{1}H NMR spectrum

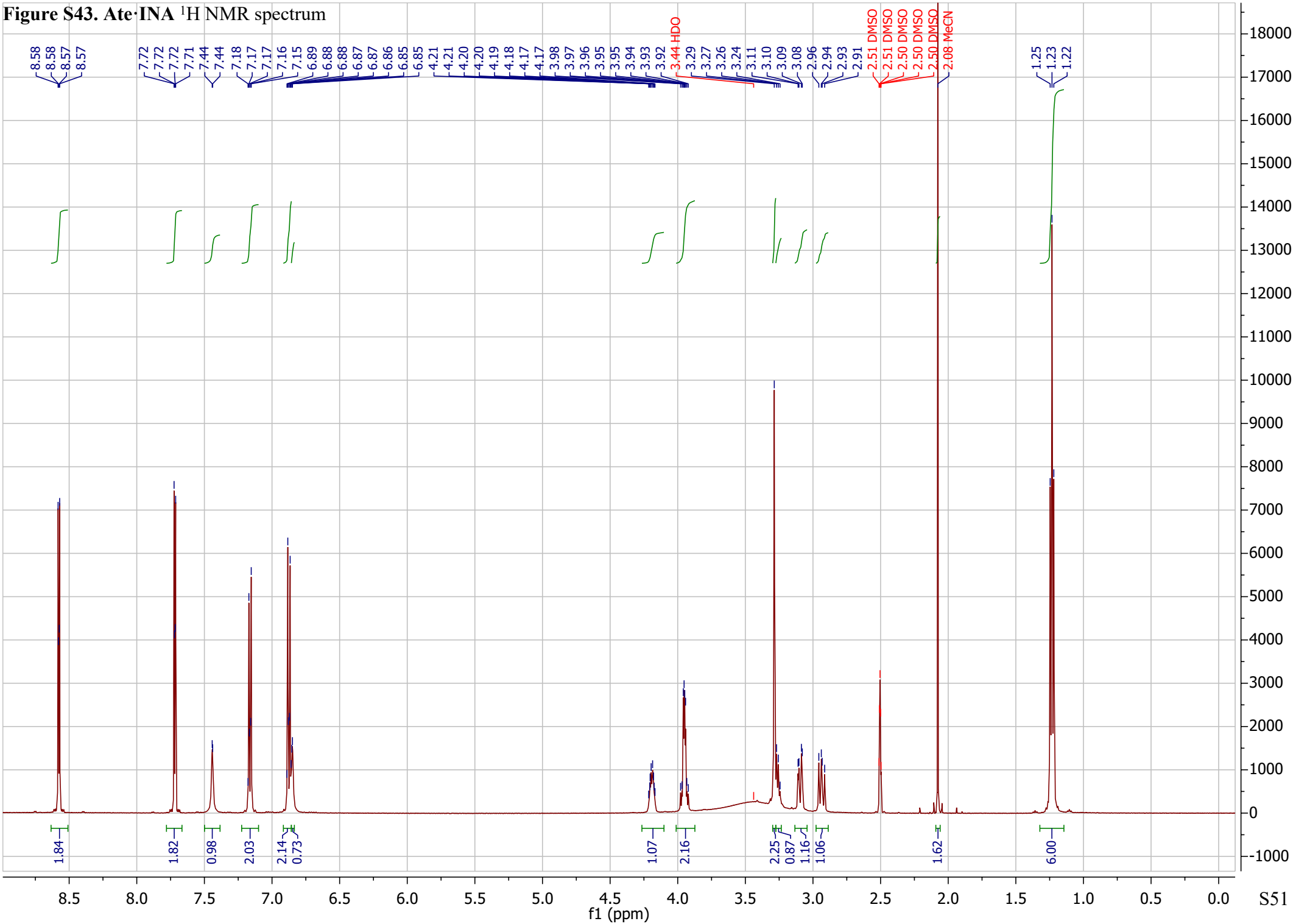

Figure S44. Lab·INA ^{1}H NMR spectrum

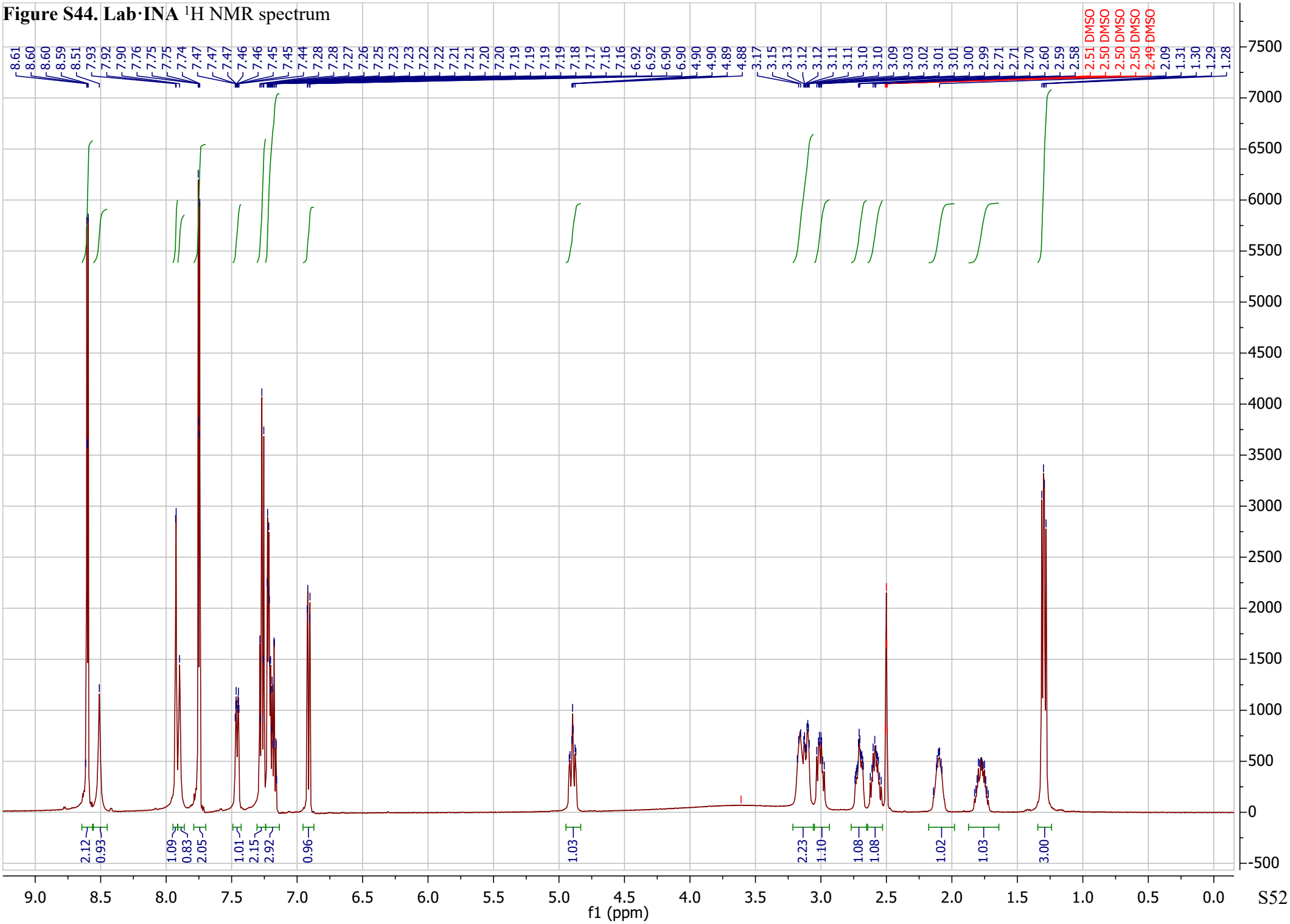

7. Thermogravimetric analysis (TGA)

TGA was performed on a TA Instruments TGA Q50 operating under a nitrogen atmosphere (40 mL/min) with a platinum pan. Powdered samples were run at a rate of 10 °C/min.

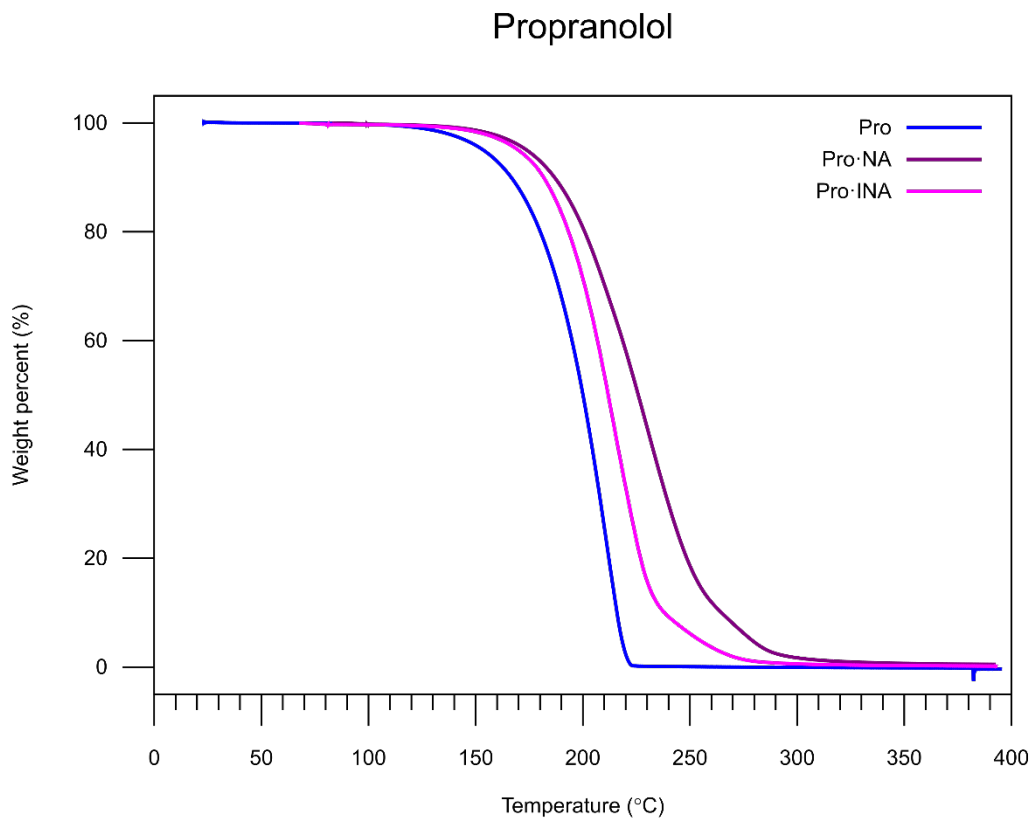

Figure S45. TGA thermograms of **Pro**, **Pro·NA**, and **Pro·INA**. Decomposition began at approximately 118, 142, and 135 °C, respectively.

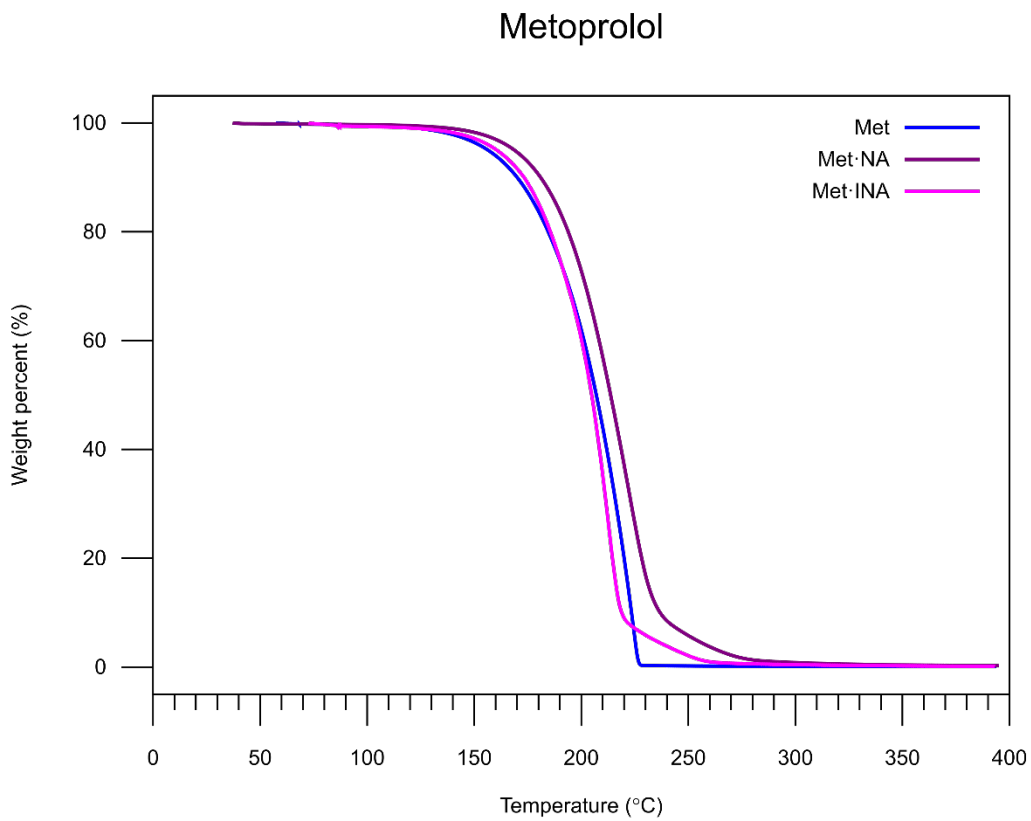

Figure S46. TGA thermograms of **Met**, **Met·NA**, and **Met·INA**. Decomposition began at approximately 123, 131, and 133 °C, respectively.

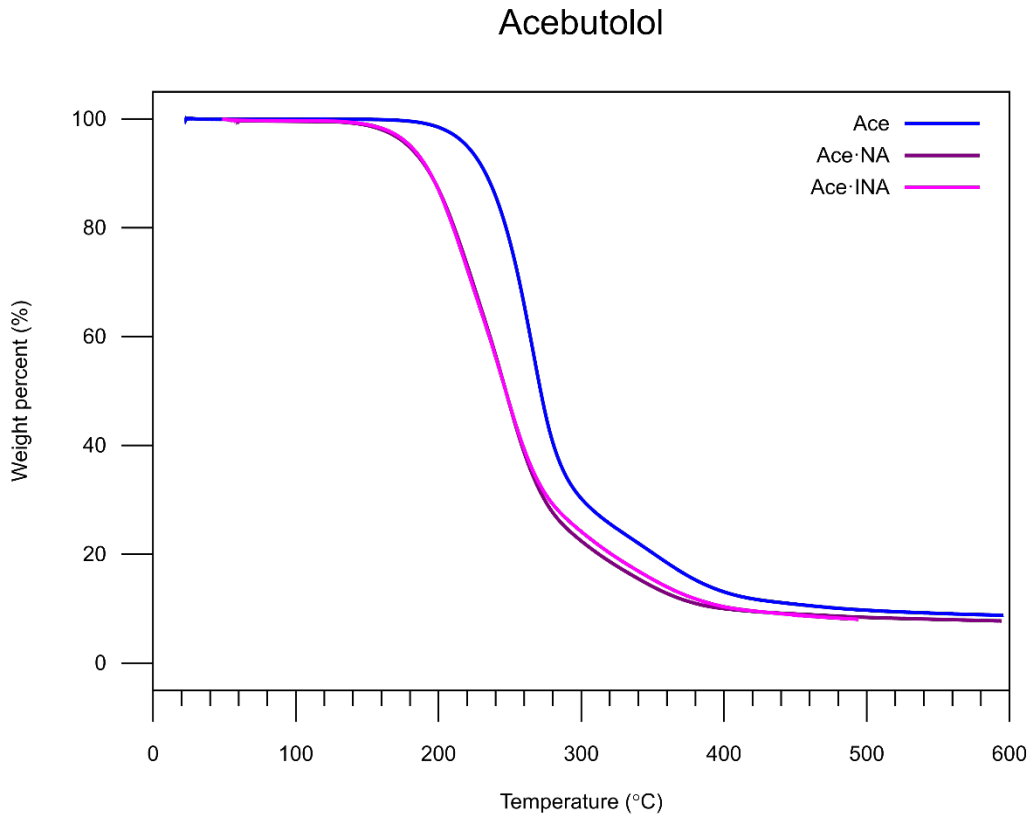

Figure S47. TGA thermograms of **Ace**, **Ace·NA**, and **Ace·INA**. Decomposition began at approximately 183, 145, and 141 °C, respectively.

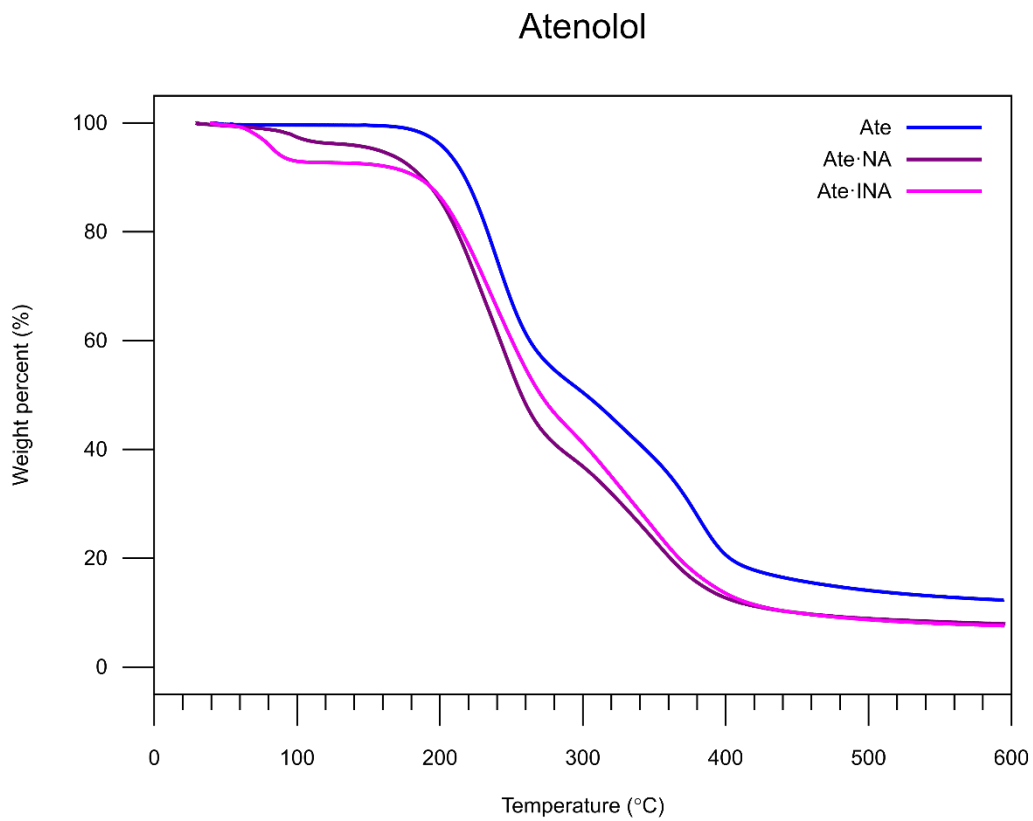

Figure S48. TGA thermograms of **Ate**, **Ate·NA**, and **Ate·INA**. Decomposition began at approximately 176, 161, and 171 °C, respectively. For **Ate·NA**, a loss of 3.3% for MeOH was observed at 123 °C (theoretical 7.6%). For **Ate·INA**, a loss of 7.4% was observed at 138 °C (theoretical 9.5%). These weight losses are lower than the theoretical amounts since the samples were mechanochemically prepared powders where less solvent incorporation is expected.

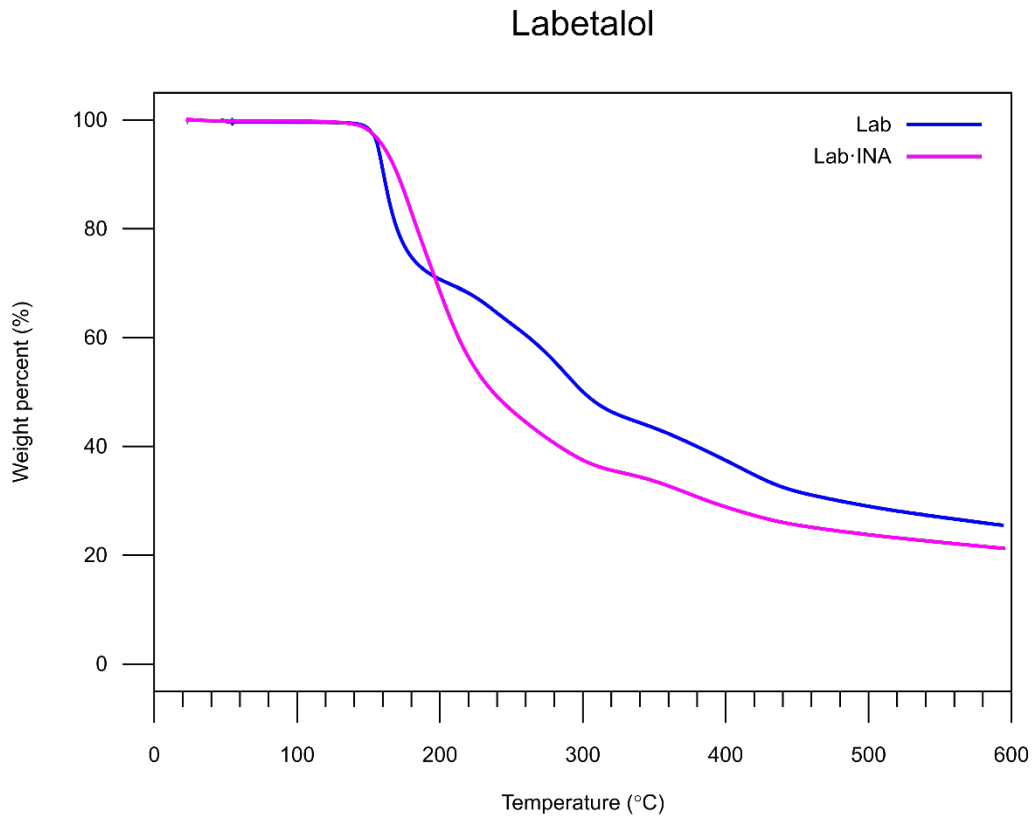

Figure S49. TGA thermograms of **Lab** and **Lab·INA**. Decomposition began at 136 and 135 °C, respectively.

8. Differential Scanning Calorimetry (DSC)

DSC experiments were performed on a TA Instruments DSC250 equipped with a RCS 90 refrigerated cooling system and under a nitrogen atmosphere (50 mL/min). Powdered samples were run at a rate of 10 °C/min in aluminum pans sealed with hermetic lids.

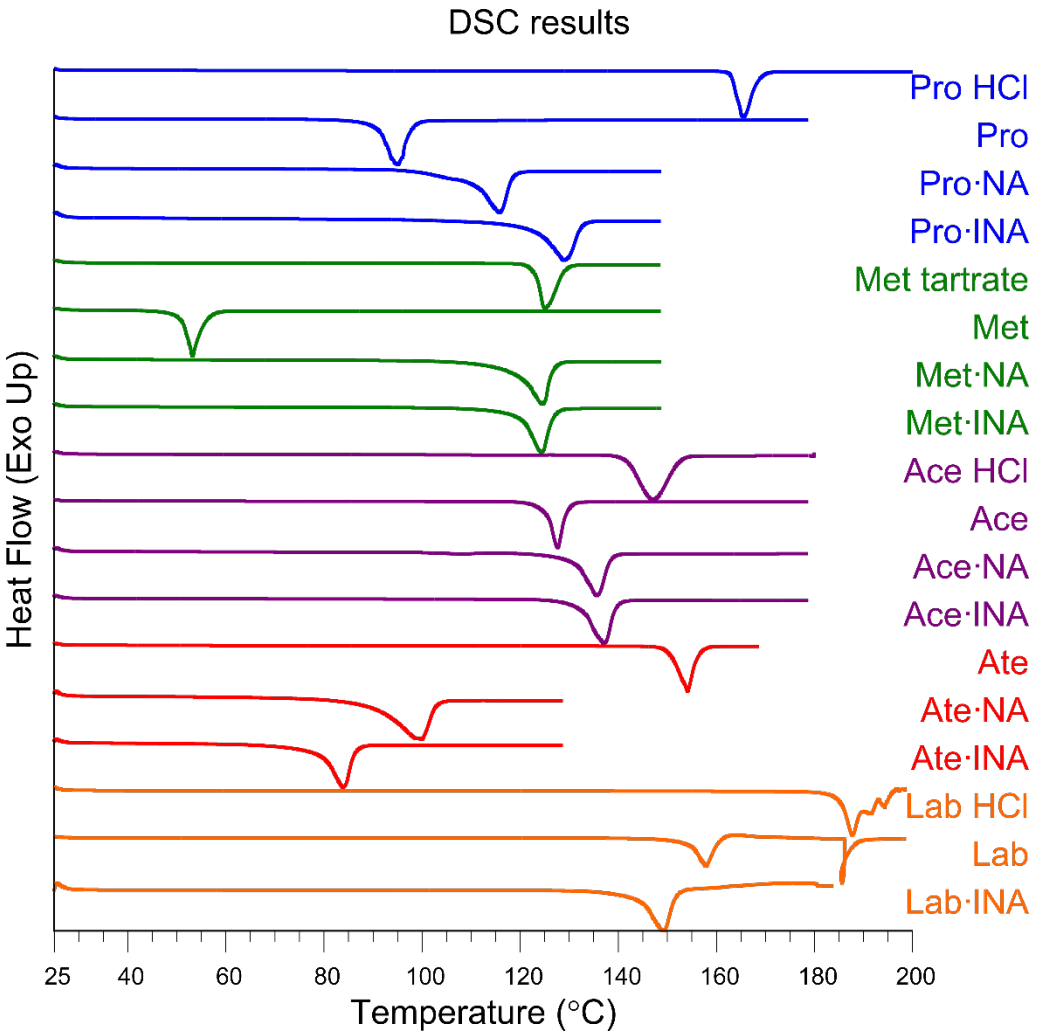

Figure S50. DSC scans illustrating the melting points of the beta blocker commercial forms, their free bases, and the **NA** and **INA** salts.

Table S11: Melting point ranges of the materials studied as determined by DSC

Material	Melting point range (°C)
Pro HCl	163-166
Pro (free base)	90-95
Pro·NA	113-116
Pro·INA	125-129
Met tartrate	121-125
Met (free base)	50-53
Met·NA	120-124
Met·INA	120-124
Ace HCl	142-147
Ace (free base)	125-127
Ace·NA	130-135
Ace·INA	132-137
Ate (free base)	150-154
Ate·NA	91-100
Ate·INA	80-84
Lab HCl	185-188
Lab (free base)	155-157, 185
Lab·INA	145-149

9. References

1. A. A. Bredikhin, D. V. Savel'ev, Z. A. Bredikhina, A. T. Gubaidullin and I. A. Litvinov, *Russ. Chem. Bull.*, 2003, **52**, 853-861.
2. H. L. Ammon, D. B. Howe, W. D. Erhardt, A. Balsamo, B. Macchia, F. Macchia and W. E. Keefe, *Acta Crystallogr. B*, 1977, **33**, 21-29.
3. K. Bialek, Z. Wojnarowska, M. Skotnicki, B. Twamley, M. Paluch and L. Tajber, *Pharmaceutics*, 2021, **13**, 2125.
4. D. Stepanovs, M. Jure, A. Yanichev, S. Belyakov and A. Mishnev, *CrystEngComm*, 2015, **17**, 9023-9028.
5. A. A. Bredikhin, Z. A. Bredikhina, A. T. Gubaidullin, D. B. Krivolapov and I. A. Litvinov, *Mendeleev Commun.*, 2004, **14**, 268-270.
6. M. Gadret, M. Goursolle, J. M. Leger and J. C. Colleter, *Acta Crystallogr. B*, 1975, **31**, 1938-1942.
7. Y. Barrans, M. Cotrait and J. Dangoumau, *Acta Crystallogr. B*, 1973, **29**, 1264-1272.
8. S. Franklin, T. Balasubramanian, K. Nehru and Y. Kim, *J. Mol. Struct.*, 2009, **927**, 121-125.
9. K. Bialek, Z. Wojnarowska, B. Twamley and L. Tajber, *Int. J. Pharm.*, 2021, **602**, 120605.
10. P. Rossi, P. Paoli, L. Chelazzi, L. Conti and A. Bencini, *Acta Crystallogr. C*, 2019, **75**, 87-96.
11. M. A. Ciciliati, M. E. S. Eusébio, M. R. Silva, É. T. G. Cavalheiro and R. A. E. Castro, *CrystEngComm*, 2019, **21**, 4319-4328.
12. W. Xing, C. Xing, M. Liu, H. Yu, B. Zhang, S. Yang, N. Gong, Y. Lu and G. Du, *J. Mol. Struct.*, 2023, **1291**, 136029.
13. P. Rossi, P. Paoli, L. Chelazzi, L. Conti and A. Bencini, *Cryst. Growth Des.*, 2018, **18**, 7015-7026.
14. G. Bartolucci, B. Bruni, S. A. Coran and M. Di Vaira, *Acta Crystallogr. E*, 2009, **65**, o1364-1365.
15. P. Paoli, P. Rossi, E. Macedi, A. Ienco, L. Chelazzi, G. L. Bartolucci and B. Bruni, *Cryst. Growth Des.*, 2016, **16**, 789-799.
16. A. Carpy, M. Gadret, D. Hickel and J. M. Leger, *Acta Crystallogr. B*, 1979, **35**, 185-188.
17. H. A. Ghabbour and G. A. E. Mostafa, *Z. Kristallogr. NCS*, 2017, **232**, 185-187.
18. R. A. Esteves de Castro, J. Canotilho, R. M. Barbosa, M. R. Silva, A. M. Beja, J. A. Paixão and J. S. Redinha, *Cryst. Growth Des.*, 2007, **7**, 496-500.
19. B. Lou, D. Bostrom and S. P. Velaga, *Acta Crystallogr. C*, 2007, **63**, o714-716.
20. E. J. Wang and G. Y. Chen, *Acta Crystallogr. E*, 2010, **67**, o91.
21. R. K. Kandula, S. B. Vepuri, H. C. Devarajegowda and S. Raja, *J. Mol. Struct.*, 2018, **1169**, 39-45.
22. J. Cai, P.-D. Liu and S. W. Ng, *Acta Crystallogr. E*, 2006, **62**, o5532-o5533.
23. P. Murray-Rust, J. Murray-Rust, D. Hartley, P. Hallett and J. Clifton, *Acta Crystallogr. C*, 1984, **40**, 825-828.
24. ChemAxon, *MarvinSketch, 23.12 pKa calculator,* http://www.chemaxon.com, 2024.
25. A. J. Cruz-Cabeza, *CrystEngComm*, 2012, **14**, 6362-6365.
26. S. L. Childs, G. P. Stahly and A. Park, *Mol. Pharm.*, 2007, **4**, 323-338.
27. Rigaku Oxford Diffraction Ltd. , *CrysAlisPro*, 2022.
28. Oxford Diffraction Ltd. , *SCALE3 ABSPACK*, 2005.
29. Bruker AXS Inc. , *APEX4*, 2005.
30. Bruker AXS Inc. , *SAINT+, (Includes XPREP and SADABS)*, 2005.
31. G. M. Sheldrick, *Acta Crystallogr. A*, 2015, **71**, 3-8.

32. O. V. Dolomanov, L. J. Bourhis, R. J. Gildea, J. A. K. Howard and H. Puschmann, *J. Appl. Crystallogr.*, 2009, **42**, 339-341.
33. G. M. Sheldrick, *Acta Crystallogr. C*, 2015, **71**, 3-8.
34. G. M. Sheldrick, *SHELXL-2018. Program for Crystal Structure Refinement. University of Göttingen, Göttingen*, 2018.
35. A. L. Spek, *Acta Crystallogr. D*, 2009, **65**, 148-155.
36. C. F. Macrae, I. Sovago, S. J. Cottrell, P. T. A. Galek, P. McCabe, E. Pidcock, M. Platings, G. P. Shields, J. S. Stevens, M. Towler and P. A. Wood, *J. Appl. Crystallogr.*, 2020, **53**, 226-235.
37. Dassault Systemes SE, *BIOVIA Discovery Studio, https://discover.3ds.com/discovery-studio-visualizer-download*, 2024.
38. S. C. Abrahams and J. L. Bernstein, *Acta Crystallogr.*, 1965, **18**, 926-932.
39. W. Arbuckle, S. Cartner, A. R. Kennedy and C. A. Morrison, *Acta Crystallogr. E*, 2009, **65**, m1232.
40. C. Reichardt and T. Welton, in *Solvents and Solvent Effects in Organic Chemistry*, 2010, DOI: 10.1002/9783527632220.app1, pp. 549-586.
41. A. F. M. Barton, *CRC Handbook of Solubility Parameters and Other Cohesion Parameters*, CRC Press, 1991.